

LASER PLASMA PARTICLE VELOCITIES

Daniel James Callahan



# NAVAL POSTGRADUATE SCHOOL

## Monterey, California



# THESIS

LASER PLASMA PARTICLE VELOCITIES

by

Daniel James Callahan

June 1976

Thesis Advisor:

Fred R. Schwirzke

Approved for public release; distribution unlimited.

T175011





## REPORT DOCUMENTATION PAGE

READ INSTRUCTIONS  
BEFORE COMPLETING FORM

1. REPORT NUMBER		2. GOVT ACCESSION NO.	3. RECIPIENT'S CATALOG NUMBER
4. TITLE (and Subtitle)  Laser Plasma Particle Velocities		5. TYPE OF REPORT & PERIOD COVERED Master's Thesis; June 1976	
7. AUTHOR(s)  Daniel James Callahan		6. PERFORMING ORG. REPORT NUMBER	
9. PERFORMING ORGANIZATION NAME AND ADDRESS Naval Postgraduate School Monterey, California 93940		8. CONTRACT OR GRANT NUMBER(s)	
11. CONTROLLING OFFICE NAME AND ADDRESS Naval Postgraduate School Monterey, California 93940		10. PROGRAM ELEMENT, PROJECT, TASK AREA & WORK UNIT NUMBERS	
14. MONITORING AGENCY NAME & ADDRESS (if different from Controlling Office) Naval Postgraduate School Monterey, California 93940		12. REPORT DATE June 1976	
		13. NUMBER OF PAGES 126	
		15. SECURITY CLASS. (of this report)  Unclassified	
		15a. DECLASSIFICATION/DOWNGRADING SCHEDULE	
16. DISTRIBUTION STATEMENT (of this Report)  Approved for public release; distribution unlimited.			
17. DISTRIBUTION STATEMENT (of the abstract entered in Block 20, if different from Report)			
18. SUPPLEMENTARY NOTES			
19. KEY WORDS (Continue on reverse side if necessary and identify by block number)  Laser; laser damage; laser operation; plasma; plasma velocities.			
20. ABSTRACT (Continue on reverse side if necessary and identify by block number)  Experiments were performed on laser produced plasma from aluminum target discs in a vacuum chamber at pressures a few times $10^{-6}$ torr. Plasma analysis was achieved using a floating double electrostatic probe of tungsten wires biased at -15 volts DC. In analyzing 376 oscilloscope trace pictures of the probe signal, four velocity signals occurred with regularity. The plasma velocities detected by the probe were determined to be $3.7 \times 10^7$ cm/sec, $1.5 \times 10^7$ cm/sec, $5.6 \times 10^6$ cm/sec (the bulk of the plasma), and			



$4.0 \times 10^6$  cm/sec. A fifth, very fast signal at  $1.0 \times 10^8$  cm/sec was also detected, but it was not consistently present. Investigation of the velocity distributions as a function of time showed them not to be Boltzmann distributions but exponential power distributions.

Investigation of the crater formed by each laser pulse resulted in the determination of the following crater dimensions; crater depth 0.01 cm/shot, crater diameter of 0.11 cm and a total spot size diameter of 0.70 cm for the laser-target interaction.



LASER PLASMA PARTICLE VELOCITIES

by

Daniel James Callahan  
Lieutenant, United States Navy  
B.S., United States Naval Academy, 1970

Submitted in partial fulfillment of the  
requirements for the degree of

MASTER OF SCIENCE IN PHYSICS

from the  
NAVAL POSTGRADUATE SCHOOL  
June 1976



## ABSTRACT

Experiments were performed on laser produced plasma from aluminum target discs in a vacuum chamber at pressures a few times  $10^{-6}$  torr. Plasma analysis was achieved using a floating double electrostatic probe of tungsten wires biased at -15 volts DC. In analyzing 376 oscilloscope trace pictures of the probe signal, four velocity signals occurred with regularity. The plasma velocities detected by the probe were determined to be  $3.7 \times 10^7$  cm/sec,  $1.5 \times 10^7$  cm/sec,  $5.6 \times 10^6$  cm/sec (the bulk of the plasma), and  $4.0 \times 10^6$  cm/sec. A fifth, very fast signal at  $1.0 \times 10^8$  cm/sec was also detected but it was not consistently present. Investigation of the velocity distributions as a function of time showed them not to be Boltzmann distributions, but exponential power distributions.

Investigation of the crater formed by each laser pulse resulted in the determination of the following crater dimensions; crater depth 0.01 cm/shot, crater diameter of 0.11 cm and a total spot size diameter of 0.70 cm for the laser-target interaction.





## TABLE OF CONTENTS

ACKNOWLEDGEMENT.....	8
I. INTRODUCTION.....	9
II. RECENT RELATED RESEARCH.....	12
III. THEORY.....	25
IV. EXPERIMENTAL DESIGN.....	31
V. RESULTS.....	51
A. CRATER DIMENSIONS.....	51
B. PROBE SIGNAL CHANGE ASSOCIATED WITH THE FIFTEENTH LASER SHOT.....	52
C. PLASMA ELECTRON TEMPERATURE.....	53
D. PLASMA DENSITY RESULTS.....	54
E. VELOCITY DISTRIBUTION ANALYSIS OF THE PROBE SIGNALS.....	55
F. PLASMA PARTICLE VELOCITY GRAPHICAL RESULTS...	60
G. OTHER VELOCITY RESULTS.....	70
H. COMPOSITE PROBE RESPONSE.....	71
VI. CONCLUSIONS.....	74
VII. FURTHER RESEARCH.....	76
APPENDIX A: THE LASER SYSTEM.....	79
APPENDIX B: THE DOUBLE ELECTROSTATIC PROBE.....	104
APPENDIX C: THE COMPUTATIONAL ANALYSIS OF DATA.....	112
LIST OF REFERENCES.....	121
INITIAL DISTRIBUTION LIST.....	126
LIST OF FIGURES.....	6



## LIST OF FIGURES

1.	The Time Delay Cables.....	32
2.	The Laser-Target Interaction Crater.....	34
3.	Laser-Target Impact Angle.....	36
4.	The Probe Distance Scale.....	37
5.	The Probe Response with the Probe 2 cm from the Target Surface.....	39
6.	Data Photo Using a 62 nsec Time Delay Cable.....	40
7.	Time Reference on a 200 nsec/cm Time Scale.....	43
8.	The Plasma Probe Signal on a 500 nsec/cm Scale.....	44
9.	The High Frequency Noise Signal Superimposed on the Laser Pulse Signal.....	47
10.	Data Photo for Graph of Ion Velocity Distribution...	56
11.	Graph of an Ion Velocity Distribution.....	59
12.	Graph of Computer Analysis Results.....	62
13.	Graph of the Plasma Velocities.....	63
14.	Graph of $\ln(n_i)$ versus $v_i^2$ .....	64
15.	Graph of $\ln[\ln(n)]$ versus $\ln(v^2)$ .....	65
16.	Average Electrostatic Probe Response Signal.....	73
17.	Block Diagram of the Laser System Components.....	80
18.	The Laser Pulse Shape.....	81



19.	The Signal Attenuator.....	83
20.	The Nd:Glass Laser Subsystem.....	85
21.	The Detector Subsystem.....	87
22.	A Floating Double Probe.....	88
23.	The Vacuum Chamber Subsystem.....	92
24.	Roughing Valve Operation.....	93
25.	Dual Relay Interlocks (W,K) for Diffusion Pump Operation.....	95
26.	Double Electrostatic Probe Circuit Diagram.....	108
27.	Data Cards Used for Data Input.....	114
28.	Computer Program Section One.....	116
29.	Computer Program Section Two and Section Three.....	117
30.	Computer Program Section Four.....	118
31.	Computer Program Section Five.....	119
32.	Computer Program Section Six and Subroutine AVENER..	120





## ACKNOWLEDGEMENT

I would like to acknowledge the valuable help and considerable patience of the Physics Department Technical Staff in carrying out this research. Particularly I would like to thank Hal Herreman, Bob Sanders, and Tom Maris for their assistance in the operation of experimental equipment and their quick response when problems arose.

Special thanks to Professors Fred Schwirzke and Alf Cooper for their academic assistance and considerable professional ability. They both lent a continuity of thought to this thesis that gave a feeling of worth to my research effort.

My thanks to the personnel at the W. R. Church Computer Center who assisted greatly in my data reduction effort and provided assistance in punching cards to put this thesis on an automatic program for reproduction. Individuals who were especially helpful; Edwin Donnellan, Joanna Jackiewicz, and Bernadette Peavey.

Invaluable help from fellow thesis students facilitated daily testing of hypotheses. Special thanks to Syd Shewchuk, John Jacobson, Fred Marcell and Francis Williamsen for those few minutes each day spent listening to proposals about experimental results or ideas for new experiments.

Lastly I would like to express thanks to my wife, Connie, for her considerable moral support, thesis typing, and draft proof reading. Her understanding of the necessity of my work was truly appreciated.



## I. INTRODUCTION

Laser plasma production has been of interest to researchers since the early days of laser study. The use of the laser as a scientific instrument quickly drew the attention of the academic community. Laser-target interaction was soon a topic of considerable research effort. Industrial and military applications of laser-dominated technology are considerable. Most recently it has been employed in research to develop the fusion reactor as an efficient, controllable source of energy, to develop a rapid, secure communication system, and to develop the much publicized laser weapon systems of future warfare. The effects of high power laser interaction with matter include (1) heating [42], (2) melting, (3) vaporization of solid materials, (4) emission of charged particles, (5) emission of neutral particles [54,11], (6) plasma production, (7) electrical discharge in gases produced by high energy laser interaction, and (8) application of these effects to material processing.

Addressing laser interaction with solid materials, particularly metals, the mechanism of the interaction has been the subject of research for over ten years. It is now understood that in metal targets struck by a laser beam, some of the light energy is absorbed by the electrons and a large part is reflected, the amount of reflection being dependent on the target material [42]. The amount of radiation energy and the time-length of the laser pulse striking the target are the controlling parameters that determine the results of the interaction.

The electrons in the conduction band will be excited to a higher energy level as incident photons are absorbed.



The energy from these interactions is transferred through collisions in the target material to other electrons and ions. The mean collision time for the electrons is one-tenth picosecond, so it is apparent that many collisions can occur in the time of a laser pulse measured in nanoseconds. The photon energy is, for all practical considerations, instantly turned to heat through particle collisions, rapidly heating a small quantity of material to very high temperatures. A laser-target interaction of sufficient energy will produce a plasma that is a dense cloud of ionized particles. Plasma production occurs at laser irradiances of the order of  $10^9 \text{ W/cm}^2$  and greater [42].

The early response of the laser produced plasma has marked characteristics that are in need of further study. The plasma plume develops quickly after the laser pulse strikes the target. The plume development is at least partially described by computer analysis at Lawrence Livermore Laboratories [32], Sandia Laboratories, and Naval Research Laboratory [37,38]. The Naval Research Laboratory in Washington, D.C. has a computer model based on a coupled system of hydromagnetic equations in cylindrical coordinates including self-generated field effects, rate equations, radiation transport, frequency diffusion of incident photons and radiation pressure [37].

The early response of the laser produced plasma which precedes the formation of the main plume is more difficult to explain [52]. It is hypothesized through experimental observation that there are four possible sources of fast propagating early signals: laser induced electron emission [52,62], fast plasma blowoff [24], electromagnetic signals, and ionization of the background gas by plasma produced photons [27] or ionizing potential waves [20].



This study was undertaken to develop further understanding of the origin of the early plasma emission through experimental study of the velocities of plasma features.





## II. RECENT RELATED RESEARCH

The newness of laser produced plasma research has not yet produced many comprehensive textbooks on the subject. Most of the literature is in the scientific journals. The most comprehensive book, judging by the number of times it is referenced by other authors and the extensive bibliography it contains, is ref. [42] by J. F. Ready. It is five years old and provides reference to most of the published articles on laser effects prior to 1971. It contains two chapters directly related to laser target interaction with a metal surface and several more chapters covering other target materials, i.e., gases, transparent material, semi-conductors, and non-metallic solids. Chapter Three, "Effects Caused by Absorption of Laser Radiation at Opaque Surfaces," discusses investigations into heating without thermodynamic phase change, laser induced melting and laser produced vaporization.

Laser induced heating without phase changes is basically a discussion of temperature change using classical thermodynamics formalism. The laser photons interact with the electrons in the solid and distribute their energy through the metal. The mean free time for collisions between electrons in a conducting metal is of the order of  $10^{-13}$  seconds. The laser radiation energy of a Q-switched or normal pulsed laser is slowly deposited ( $t=10^{-8}$  seconds as compared to the electron mean free collision time of  $10^{-13}$  seconds). A condition of thermal equilibrium can be assumed to exist.

J. H. Eichel also has investigated laser-induced



temperature changes of the absorbing media [8] but at incident irradiances such that neither melting nor vaporization occurs. Here the heat-conduction equation

$$\nabla \cdot \vec{J}(r,t) + \rho c \frac{\partial T(r,t)}{\partial t} = A(r,t)$$

is solved and is called the volume generation model, in which  $T$  is a temperature function,  $\vec{J}$  is the thermal energy crossing a unit area per unit time,  $\rho c$  is the heat capacity per unit volume and  $A$  is the net energy per unit volume per unit time generated within the solid. An alternative method of formulating the problem of laser heating of absorbing material is called the surface generation model. In this solution the heat is assumed to be generated on the surface of the target and the homogeneous heat-conduction equation is solved with boundary conditions at the irradiated surface. Experimental evidence is derived for  $\text{CO}_2$  laser

radiation impinging on a tungsten target to agree with the theory developed [8]. The surface generation model can be used to predict laser-induced temperature changes produced by pulsed lasers. For very short pulsed, picosecond, mode-locked solid state and dye lasers the volume generation model is more accurate.

The no-phase-change laser heating problem is addressed by J. T. Schrieffer [39]. He solves the heat flow equation for a semi-infinite solid and a slab of finite thickness (thin film) and compares the results to experimental observations on aluminum and stainless steel. R. A. Ghez and R. A. Laff [21] have reported on laser heating of thin films. The problem is solved using the one dimensional heat flow equation. A numerical example for a silicone film on a silica substrate illuminated with a CW argon-ion laser is compared with experimental observations by Ghez and Laff.



Ready [42] continues in Chapter Three with laser-induced melting and a theoretical solution using the heat equation. Melting or reducing a solid to its liquid phase without vaporizing it requires a very fine energy division when using a laser energy source. The pulsed lasers are not especially suited for that application, but CW lasers which can be adjusted to variable energies are well suited for melting. Schriempf [39] works the semi-infinite slab melting problem theoretically by use of the simple heat flow equation

$$\frac{\partial^2 T}{\partial z^2} - \frac{1}{\kappa} \frac{\partial T}{\partial t} = 0$$

assuming the melted material is immediately removed. This is a realistic assumption demonstrated by J. A. Fox [19]. Fox showed that two lasers (one pulsed and one CW) can provide a workable technique to clear the molten target material away rapidly enough to consider it as being removed immediately. Ghez and Laff [21] address laser melting of a film and substrate as a three-phase Stefan problem of liquid film, solid film, and substrate. The Stefan problem is one in which a given material transforms from one thermodynamic phase to another with the emission or absorption of heat [12]. Assumptions are made to remove analytical difficulties that make the problem otherwise insoluble. The solution to the problem is found by the simple heat flow equation as in Schriempf's work.

Considerable attention is given to laser-induced target vaporization and plasma production in the scientific literature. It is probably the most important aspect of laser-target interaction when consideration is given to the ever more energetic laser pulses and the shorter pulse widths of state-of-the-art lasers. Vaporization and plasma production are of direct interest to scientists attempting to design fusion reactors who need to know exactly what is





happening at the fuel surface when the laser beams strike the deuterium-tritium fuel pellet [29]. Vaporization of the target material is very readily attained with pulsed and Q-switched lasers. Ready [42] emphasizes the experimental measurements of material removal and some methods of calculating it. There is a great difference between the behavior of a target surface struck by a millisecond laser pulse and a target surface struck by a nanosecond or picosecond pulse. Intense, short laser pulses do not produce much vaporized material removing only a small amount of target material from the target surface with high flux density. Longer lower-powered pulses from a normal pulsed laser on the other hand produce deep, narrow holes in the target. Experimental data on the amount of material vaporized by a laser pulse is not very reproducible. It is dependent on exact duplication of experimental conditions and even the laser pulse is only reproducible to within  $\pm 20\%$  of the rated energy from pulse to pulse on many high power lasers. Ready [42] presents several graphs of laser crater depth versus laser flux density ( $\text{W/cm}^2$ ) and laser energy output (Joules). The heat flow equation is used to give a quick, simple estimate of the depth of vaporization. As the target material vaporizes, the thermodynamic phase changes that take place invalidate the heat equation for all but rough estimates. The thermal conductivity, heat capacity, and density are all temperature dependent. The reflectivity is temperature and thermodynamic phase dependent. The laser-target crater depth is therefore not actually a simple function of position and temperature as the heat equation indicates.

One model of the processes involved in vaporization by a Q-switched laser considers the pressure produced by the production of a small amount of blowoff material early in the laser pulse. This recoil pressure raises the boiling



temperature of the target above the normal atmospheric pressure vaporization temperature. If then, one considers that the increase in vaporization temperature of the surface material is sufficiently high, the surface will be prevented from vaporizing further and the material will continue to heat to a temperature above normal vaporization temperature as laser light continues to be absorbed by the target surface. The target surface will eventually reach the critical point where vaporization can occur. This model gives reasonable agreement with experimental observations for one range of laser flux density ( $10^9 \text{ W/cm}^2$ ). It makes no allowances for shielding or partial shielding of the target surface from the laser beam at the target spot as the blowoff material (plasma plume) becomes hot, ionized, and opaque.

At sufficiently high laser power density the blowoff can be assumed to be a plasma. Gas dynamics, plasma absorption mechanisms, thermal ionization processes and reradiation by the plasma are all included in a model given by Ready [42]. This model predicts experimental facts with relatively good accuracy. Graphs for vaporization depth (crater depth) as a function of energy density [ $\text{J/cm}^2$ ], velocity of surface vaporization [ $\text{cm/sec}$ ] vs. laser flux density [ $\text{W/cm}^2$ ], target surface temperature as a function of laser flux density and vaporization depth versus laser pulse duration are presented for comparisons.

These models each emphasize a particular aspect of the interaction. They each give a reasonable treatment of one of several phenomena, but there are no comprehensive models that compile all of the phenomena into a single solvable model.

Continuing, Schriempf [39] presents a solution to the problem of uniform continuous laser irradiation of a solid



target; the one dimensional problem. The melted volume of the target is assumed to be in place until it reaches vaporization temperature, when it is assumed to evaporate completely. The pulsed laser situation for laser radiation is assumed. This is not an unreal situation as demonstrated by Fox [19]. One is usually interested only in power densities below the breakdown threshold of air because at higher power densities the energy cannot reach the target if it is in the ambient atmosphere. The breakdown levels are a function of laser radiation wavelength, spot size, laser pulse length, laser pulse shape and the contaminants in the atmosphere (i.e., smog, fog, chemicals, smoke and humidity). It is for this reason that most experiments concerning laser-target interaction are done under at least partial vacuum conditions. High power density laser pulses are considered by Schriepf [39] in laser-target interactions assuming that the plasma blowoff does not shield the target spot from the laser radiation. In addition to the thermal change to the target, there is a strong pressure built up on the target surface due to recoil from the vapor blowoff. This is where the spall and deformation of the target surface is suspected to come from. A crater of much smoother geometrical shape can be produced with a two laser system which removes the melted material quickly before it can vaporize and set up a shock front [19]. A theoretical calculation is done for the semi-infinite slab and numerical examples are carried out for titanium and aluminum [39].

R. A. Clstad and D. R. Clander [40] in a study of the vaporization of iron by a laser pulse, have used the transient heat conduction equation to solve the laser-interaction problem. Two assumptions are made in this work: (1) heat conduction occurs only in a direction normal to the target surface, and (2) because metals are opaque to visible light, the laser radiation is represented by a surface heat source. The temperature and time histories of the solid during a pulse may be compared by solution of the





transient heat equation. First, the surface temperature rises, melting and vaporizing the target. Neutral atoms or molecules are emitted into the gas or vacuum around the solid. If the surface temperature exceeds the melting point of the substrate, rapid vaporization of the melt occurs and the escaping vapor exerts a recoil pressure on the liquid which causes it to flow outward along the surface. This movement of liquid is observable as a crater at the point of impact of the laser radiation. The recoil pressure into the solid target, when using laser beam energy densities of  $10^9$  (W/cm<sup>2</sup>) and greater, is enough to eject small globules of molten metal in a direction away from the target surface.

P. S. F. Wei, D. J. Nelson, and R. B. Hall [59] present a simple model for evaporation in which the surface temperature is raised according to its heat capacity, the absorbed energy and the heat conductivity to the bulk. When the vapor pressure becomes comparable to that of the surrounding atmosphere, surface boiling begins. In the absence of superheating, the evaporated particles velocity would obey the three-dimensional Boltzmann distribution.

For plasma production, Ready [42] and Huddleston and Leonard [25] both have a good review of the different techniques used in experimentation to investigate the characteristics of the plasma plume in high energy laser-target interactions. Photographic techniques, interferometric techniques, optical spectroscopic studies, X-ray emission, charge collection measurements with shielded probes, pressure pulses, and magnetic field considerations are all briefly described by Ready and in greater detail by Huddleston with much attention to extensive bibliographies to support each method.

Laser-target interaction can be characterized by two conditions at the impact area. The first is a low temperature region where the target material is barely





icrized and the second a high temperature region where the target material is in a plasma state [30]. In the low temperature region the target material is in the process of changing thermodynamic states from solid to vapor. The phase transitions are characterized by a strong, dynamic transition from one state to another in a short period of time. In the high temperature region a hot plasma is produced that expands to form the plasma plume in a direction away from the impact area. The velocity of the expansion and the composition of the expanding plasma are areas of much concern to researchers.

Laser produced plasma particle velocities are the basis of this thesis. The following is a summary of some of the research done on laser produced plasma particles to date and the findings using various diagnostic techniques. Dextroder and Jantz [17] found, using a tetrode screen detector system, that the velocity of hydrogen ions in a laser induced plasma blowoff was  $4 \times 10^7$  cm/sec with a 500 MW incident laser power, carbon ions had a velocity of  $1.6 \times 10^7$  cm/sec for a 200 MW incident laser power, and copper ions had a velocity of  $10^7$  cm/sec also for incident power equal to 200 MW. A Q-switched ruby laser was used in these experiments with a pulse width of 30 nsec. The incident power densities ranged up to  $5 \times 10^{11}$  W/cm<sup>2</sup>. The detector was placed 170 cm from the target.

Inoue, Kawasumi, and Miyamoto [26] found plasma particle velocities an order of magnitude smaller for carbon ions using an ion energy analyzer. A ruby laser was used in these experiments with a maximum power of 80 MW and total energy 1.2 J. The target was a polyethylene  $(CH_2)_n$  filament. The only species they detected in the plasma was



$C^{2+}$ . Two velocities were determined (parallel velocity and lateral velocity) for the carbon ions,  $3.4 \times 10^6$  cm/sec and  $1.5 \times 10^6$  cm/sec.

Gregg and Thomas [23] used a Q-switched ruby laser with power densities from  $1.5 \times 10^{10}$  to  $5 \times 10^{11}$  W/cm<sup>2</sup>. They experimented using lithium hydride (LiH), lithium, beryllium, carbon, sulfur, aluminum, zinc, and silver targets. For each target material a graph was plotted of the log of the ion velocity squared [cm<sup>2</sup>/sec<sup>2</sup>] versus the log of flux density [W/cm<sup>2</sup>]. The ion detector was a photomultiplier tube 40 cm from the target. An analytical relationship was discovered for the ion velocities of each target material. It was found by graphical analysis that

$$(v)_{avg}^2 = AE^x \quad \text{and,}$$

$$(v)_{max}^2 = BE^y$$

given E equal to the peak intensity of the laser pulse in W/cm<sup>2</sup> from about  $1.5 \times 10^{10}$  to  $5 \times 10^{11}$  and A, x, B, and y are given by the following table.



Table 1.

Material	x	y	A	B
IiB	0.459	0.540	$2.12 \times 10^9$	$5.05 \times 10^8$
Ii	0.425	0.533	$3.99 \times 10^8$	$4.93 \times 10^8$
Fe	0.521	0.565	$4.14 \times 10^8$	$2.72 \times 10^8$
C	0.561	0.619	$1.20 \times 10^8$	$5.48 \times 10^7$
S	0.469	0.627	$7.48 \times 10^6$	$2.72 \times 10^4$
Al	0.695	0.859	$1.90 \times 10^{10}$	$5.82 \times 10^8$
Zn	0.330	0.500	$1.06 \times 10^9$	$3.44 \times 10^9$
Ag	0.339	0.377	$6.24 \times 10^9$	$5.24 \times 10^9$

For an aluminum target their findings for ion velocities ranged from  $5 \times 10^6$  to  $1.7 \times 10^7$  cm/sec.

Reedy [43] used visual microscopic analysis of high speed photographs to determine carbon ion velocities of  $2 \times 10^6$  cm/sec. A 30 MW Q-switched laser was used for this experiment with a skewed pulse shape rising to its peak value in 10 nsec and ending at about 45 nsec.

Antonciv [2] established the ion velocity of a laser produced aluminum plasma to be between  $v_{avg} = 5.2 \times 10^6$  cm/sec

and  $v_{max} = 8.6 \times 10^6$  cm/sec. In this work a cylindrical

capacitor probe placed 90 cm from the target was used for detection. The laser used was a Q-switched Nd:glass laser with a full width half maximum pulse length of 25 nsec and an energy of 1.8J. The laser flux density was  $1.1 \times 10^{12}$

W/cm<sup>2</sup>.



Wei, Nelson, and Hall [59], through spectrographic analysis of boron nitride (BN), aluminum oxide ( $\text{Al}_2\text{O}_3$ ), and soda-lime glass targets arrived at velocities that were significantly lower than other experimenters. In table form:

Table 2. Particle Velocities in cm/sec

	MOST PROBABLE VELOCITY	AVERAGE VELOCITY	MAXIMUM VELOCITY
BN	$2.25 \times 10^5$	$2.53 \times 10^5$	$2.76 \times 10^5$
$\text{Al}_2\text{O}_3$	$1.25 \times 10^5$	$1.41 \times 10^5$	$1.53 \times 10^5$
Soda-Lime Glass	$0.73 \times 10^5$	$0.82 \times 10^5$	$0.89 \times 10^5$

For this experiment a  $\text{CO}_2$  laser was used with a 25 microsecond pulse, 15 J. of energy and a relatively low flux density of  $10^7 \text{ W/cm}^2$ . The microdensitometer detector was placed 4 mm from the laser-target impact point. The reason for the very low ion velocities in this experiment may be the low flux density of the  $\text{CO}_2$  laser used.

Fasqv, et al. [7] measured the plasma ion velocity of carbon ions with an electrical diagnostic probe in a Faraday cylinder. Their results were plasma velocities of the order of  $10^7 \text{ cm/sec}$ . They also noted the velocity of the opaque region of the plasma plume to be  $5 \times 10^5 \text{ cm/sec}$ . The laser





used was a Q-switched Nd:glass laser with a pulse length less than 15 nsec and flux density of  $10^{12}$  W/cm<sup>2</sup>. Using another detection technique, Basov, et al. [6] again provided ion velocities for the laser induced plasma. The method of plasma diagnostics used in this experiment was rather ingenious. Basov measured the optical density of the plasma with a second laser at right angles to the first, several centimeters out from the target surface. The beginning of the plasma plume was detected by shining the second laser light through the plume. The opaque region of the plasma plume was found to have a velocity of  $6.3 \times 10^6$  cm/sec for the aluminum plasma and the fast aluminum ions had velocities of the order of  $1.6 \times 10^7$  cm/sec. A Q-switched Nd:glass laser was used with 150 MW, 25 nsec pulse length.

Does any theoretical development also predict these velocities in the experimentally observed magnitudes? B. Steverding [52] in the theoretical development of target shock theory for incident laser flux greater than  $10^9$  W/cm<sup>2</sup> showed by theoretical calculations that the blowoff velocity is about  $4 \times 10^5$  cm/sec. He used a set of problem parameters similar to those in the actual experimental situation used by Wei and Hall [59]. An idealized laser pulse at 10.6 microns with an initial spike of one microsecond duration and maximum intensity of  $2 \times 10^7$  W/cm<sup>2</sup> was used in the calculations. The other parameters were target density equal to 5 gm/cm<sup>3</sup> and the speed of sound in the target material of  $2 \times 10^5$  cm/sec. The problem solution was obtained using the one-dimensional theory of shock generation and plasma formation to arrive at plasma velocities of the order



of  $4 \times 10^5$  cm/sec. The experimental results in the actual physical problem were  $4.8 \times 10^5$  cm/sec. For air pressures below 0.1 atm. a blast wave will form at laser impact rather than a detonation wave.



### III. THEORY

In laser-target interaction the question arises, what is the mechanism or mechanisms of plasma production? Many facets of the answer are as yet unexplained because of the complexity of the differential equations used to formulate a model of the problem. Laser radiation absorption by the surface of a solid metal target causes heat to be deposited in a thin surface layer of the target material. The surface temperature increases and heat waves are propagated in the target. The heat cannot diffuse out of the absorbing target layer as fast as it is being injected so the temperature continues to increase until the target material begins to vaporize.

The transition of a gas into the plasma state involves various particle interaction processes. Collisions of the particles among themselves and interactions with radiation encompass most of the energy transfer [20]. Ionization, the stripping of electrons from atoms and molecules, is accomplished by the energetic (hot) electrons colliding with atoms and molecules. The inverse of this process is recombination. The atom or molecule has to rid itself of energy. Three body recombination, in which two electrons collide simultaneously with an ion, one carrying away the excess energy and the other attaching itself, takes place in a dense plasma.

There are three basic methods of radiation emission from particle interaction in a plasma; discrete radiation, recombination radiation, and bremsstrahlung. Discrete radiation arises from electron transitions from one energy level to another in the same atom. Discrete radiation is of a single wave length. A complete picture of this form of



radiation consists of numerous spectral lines. Another term used for discrete radiation is bound-bound radiation. Recombination radiation is emitted when a free electron is captured by an ion. A lower energy state is assumed by the electron and the energy is emitted in the form of a photon. Recombination radiation is sometimes referred to as free-bound transitions. Bremsstrahlung is radiation from interaction between a free electron and an ion in which the electron is only decelerated, not captured. This is referred to as free-free radiation.

At the time of vaporization, the surface temperature of the target material will begin to depend on the rate of vaporization; that is, the evaporation mechanism. Thermal diffusion continues to increase the temperature of the dense solid and liquid states still at the target surface but ceases to play a significant role in the plasma temperature increase.

In order to develop the condition for plasma production, sufficient radiation energy density must be delivered to the target.

The electrostatic probe and associated theory was originally developed by Langmuir [31,36,55,56] and has evolved through a number of authors, Johnson and Mather [28], Eaksht [4], Lindberg [33], Virmont [58], Eyni [18], Chen [25], Swift [53], and Chung [14,15], to its present use in plasma diagnostics, from space probes to fusion reactor research. The electrostatic probe has been used as a fundamental diagnostic tool for measuring plasma characteristics. The original work in its use and theory was done by Langmuir (1924-1929) so the electrostatic probes, particularly the single filament probes are called Langmuir probes.

The electrostatic probes themselves are relatively simple devices, but the theory supporting the probe response is particularly complex (see Chen [25]). The electrostatic probe basically consists of one or more small, metallic







electrodes (whiskers) that are inserted into the plasma to be characterized. The electrodes may be cylindrical or spherical in shape, or may just be a plate or some other regular or irregular geometric shape which suits the probe surface area calculation model and does not interfere with the plasma flow or the plasma energy fields. The basic assumptions associated with electrostatic probe use, as listed by Swift [53], are:

- (1) Electron and ion concentrations in the plasma are equal.
- (2) Electron and ion mean free paths are much greater than the electrostatic probe radius for a cylindrical or spherically shaped probe.
- (3) Electron temperature in the plasma is much greater than the ion temperature.
- (4) The probe radius is much greater than the Debye length.
- (5) The electron and ion velocity distributions are Maxwellian.

In the single probe configuration, the probe operates by a single electrode inserted into the plasma and attached to a variable power supply. The power supply can be biased at various potentials, positive or negative with respect to the plasma for optimal probe signal response. Current at the probe is measured as a function of the probe potential. The other electrode (usually a plate) is a ground for the plasma. The plate is normally fixed at a conducting section of the wall of the plasma confinement vessel. In electron discharge tubes the customary experimental arrangement uses the anode of the tube as the reference electrode. The Langmuir probe must have a continuous conducting medium from the plate to the electrode which has distinct disadvantages when studying laser produced plasmas.



The double probe configuration for plasma investigation is typically two symmetric electrodes that are in contact with the plasma. The double probe was first used by Johnson and Malter [28]. The current flowing in the plasma between the two electrodes is measured as a function of the voltage applied between them. The double probe has the advantage over the single probe in that there is no net charge drain from the plasma since the two electrodes and the power supply of the double probe system form an isolated closed circuit, i.e., it is not grounded to any other equipment. Both electrodes are always negative with respect to the plasma and the maximum current drain by the probe on the plasma is limited by the ion saturation current to the surface area of the two probe whiskers.

The theory of electrostatic probes is complicated because the probe electrodes are themselves plasma boundaries. At and near the plasma boundaries the plasma characteristics are changing, usually very markedly. In other words, it is a grand dilemma. The necessity of getting inside of the plasma with a probe that is by definition outside. Charge neutrality does not hold near the plasma boundary. A thin layer called the Debye sheath [13] exists at the boundary where electron and ion number density differ from the values within the plasma and E fields are present. For a probe at plasma potential the sheath vanishes.

Chen [25] and Swift [53] have summarized the theoretical results of electrostatic probes in a systematic manner. The experimental considerations when using electrostatic probes follow.

(1) The surface of the probe whiskers should be clear of all contaminants. If the plasma temperature is lower than the work function of the probe whiskers, then the variation of the work function over the probe surface will



affect the probe characteristics. It is good procedure to outgas the probe whiskers before starting an experimental data run, if enough current is available to the circuit, by increasing the probe current enough to heat the whiskers to incandescence.

(2) Secondary emission from the probe whiskers and arcing across the whiskers can also be a problem. The effects of secondary emission are difficult to correct and can be avoided by using probe whiskers that have low emission coefficients and by using low probe circuit voltages.

(3) In a weakly ionized plasma, the presence of an electrostatic probe disturbs the nature of the plasma by lowering the plasma density in the vicinity of the probe whiskers outside of the Debye sheath around the probe. In high temperature plasmas, the probe can dissolve in the plasma, adding to the impurity problems in the plasma vessel.

(4) Using a shielded probe for plasma diagnostics introduces still another boundary to the plasma and all of the associated boundary problems. If using a shielded probe can be avoided while still satisfying the experiment design parameters, it should be.

(5) The plasma probe signal is a function of the surface area of the probe exposed to the plasma. If the plasma energy is great enough to dissolve the probe, the surface area reduction of the probe must also be taken into account in the experimental design.

(6) If the response characteristics of the probe are too slow to follow the oscillations set up in the plasma, the probe signal will be useless. An approximation of the expected plasma oscillation frequency should be made before designing the frequency response of the probe circuit.

(7) Electron reflection, that is electrons that arrive at one of the probe whiskers which reflect back into the plasma, can be a problem for accurate measurements in a





terucus plasma.

(8) Photoelectron emission by the probe must be accounted for in experiments with a very tenuous plasma. When the plasma ion currents are small, photoelectron emission can have a dramatic effect on the probe signal.

(9) In small plasma discharges, the length of the probe and the plasma perturbations induced by the probe may be large compared with the length of the gradient of the plasma ion number density. The resulting effect on the probe current must be compensated for.

(10-12) Negative ions cause the collisionless plasma theory assumptions to be invalidated, metastable atoms liberate electrons that alter the probe signal, and ions orbiting around the negative whisker of the probe all cause probe signal anomalies that must be realized in accurate plasma research.

(13) The probe circuit, external to the plasma vessel, is a part of the experimental considerations that is sometimes overlooked. Stray capacitance of the electrostatic probe leads or in the circuit wiring is of great importance when attempting to detect high frequency signals. A floating double probe system will not follow rapid changes in the plasma potential unless the entire system has a small leakage capacitance to ground. Ground loops and stray r-f signals are a particular problem around the probe circuit.

The double probe theory used in the research discussions can be found in Appendix E. A detailed formulation of the plasma temperature and density, the characteristic Debye length for the plasma, and the ion saturation current are all included in the appendix.





#### IV. EXPERIMENTAL DESIGN

In this research, the velocity of a laser-produced plasma from an aluminum disc target was investigated. It was a continuation of research questions posed by Brooks [10] and Schwirzke and Cooper [46,47]. The target was suspended in a vacuum chamber at a pressure of  $3 \times 10^{-6}$  to  $1.8 \times 10^{-6}$  torr with most data being taken at  $1.8 \times 10^{-6}$  torr. A Nd:glass laser system was used (see Appendix A) to provide a 340 MW, 25 nsec half width laser pulse. The average laser energy was  $8.6 \pm 1.5$  J for the 376 data shots that were used in determining the plasma velocities.

To calculate the time reference frame between the trigger, the pulse and the signal, two-thirds the speed of light was used as the characteristic speed of the electronic signal in the cables and the speed of light was used for the laser light in the dehumidified atmosphere of the laboratory air. The physical arrangement of the laser light path, the delay cables and the oscilloscope are given in Figure 1.

Sample calculations of the time relationship of the plasma signal to the triggering circuit gave the following: For the trigger signal path (AFGHJ), the transit time of a signal at A was 21.5 nsec. This was calculated using  $t = d/v$ , ie.,  $AG = 120$  cm,  $GJ = 350$  cm,  $c = 3 \times 10^{10}$  cm/sec (the speed of light in a vacuum).

$$\begin{aligned} AG/c + GJ/(2/3)c &= 120/3 \times 10^{10} + 350/2 \times 10^{10} \\ &= 21.5 \text{ nsec} \end{aligned}$$



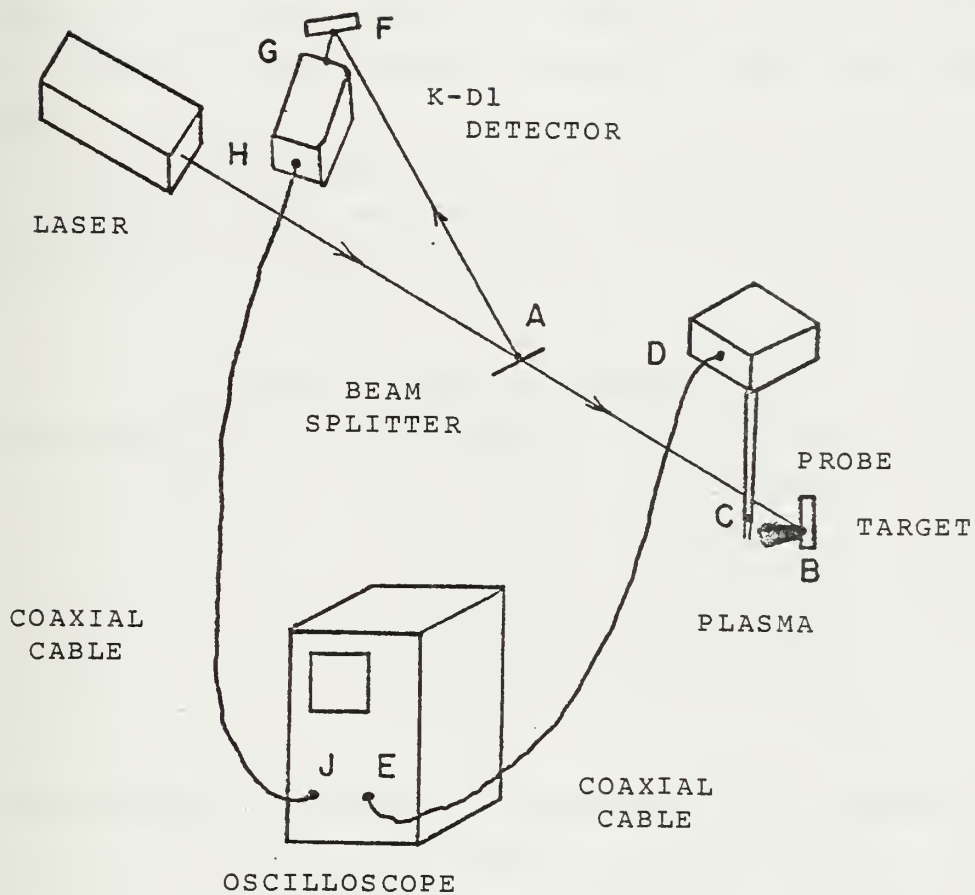


FIGURE 1. THE TIME DELAY CABLES



Similarly, the other path (AB+CDE) was calculated where  
 $AE = 60 \text{ cm}$  and  $CE = 300 \text{ cm}$ .

$$\begin{aligned} AE/c + CE/(2/3)c &= 60/3 \times 10^{10} + 300/2 \times 10^{10} \\ &= 17 \text{ nsec} \end{aligned}$$

Note that the distance BC does not appear in the calculation because that is the unknown velocity that was being measured.

When the laser beam struck the aluminum target at an angle of  $30^\circ$ , a crater was formed. Figure 2 is a graphical representation of the resulting hole.

Table 3. Crater Dimensions

Dimensions	10 Shots	25 Shots
A	0.160 cm	0.175 cm
E	0.410 cm	0.408 cm
C	0.105 cm	0.115 cm
I	0.100 cm	0.225 cm
F	0.704 cm	0.701 cm

The measurements in Table 3 were made with a caliper and micrometer. The laser pulse removed 0.01 cm of the bottom of the crater hole on each shot (dimension I divided by the number of shots). To calculate the laser flux density at the target, it was assumed that the pulse length in seconds (t) equaled the half width of the pulse (25 nsec) and the diameter (d) of the beam incident to the target was dimension C from Figure 2. Laser energy equaled 8.6 J on the average, so  $E = 8.6 \text{ J}$ ,  $t = 25 \text{ nsec}$ ,  $d = 0.110 \text{ cm}$ .

$$\begin{aligned} \text{flux density} &= E/t \pi (d/2)^2 = 8.6/25 \times 10^{-9} (0.055)^2 \\ &= 3.62 \times 10^{10} \text{ W/cm}^2 \end{aligned}$$



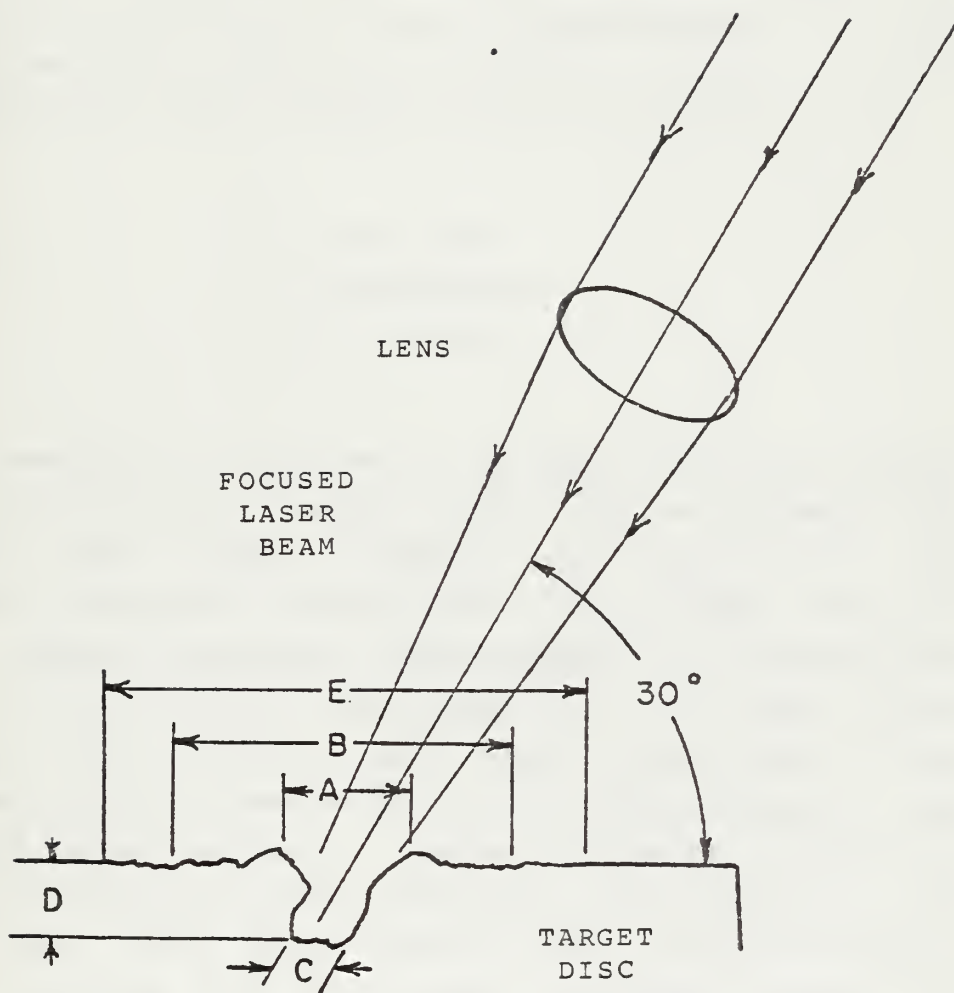


FIGURE 2. THE LASER-TARGET INTERACTION CRATER





The possibility of drilling completely through the aluminum disc had to be guarded against so that all of the laser produced plasma came out the front of the target. The thickness of the disc measured with a micrometer was 0.635 cm (0.25" machined aluminum). If  $s$  was the depth the crater must reach to drill a hole all the way through the target and each laser shot removed approximately 0.01 cm of the target material, then it was estimated that 70 to 75 shots would make a hole through the disc (see Figure 3).

$$\begin{aligned} s &= d / \cos 30^\circ \\ &= 0.635 / 0.866 \\ &= 0.733 \text{ cm} \end{aligned}$$

To measure the distance of the probe from the surface of the aluminum target, a simple bench mark arrangement was used atop the vacuum chamber (see Figure 4). The electrostatic probe was inserted in a probe holder which was bolted to a flat, rectangular brass plate. An aluminum butt plate was bolted on top of the chamber and the brass plate was marked with a bench mark about in the center of the probe. The plate was then moved so the probe whiskers just touched the target surface. A paper centimeter graph scale was matched up with the bench mark and taped down on the aluminum butt. The brass plate could then be moved a specified distance and the probe distance would be measurable to  $\pm 1$  mm.



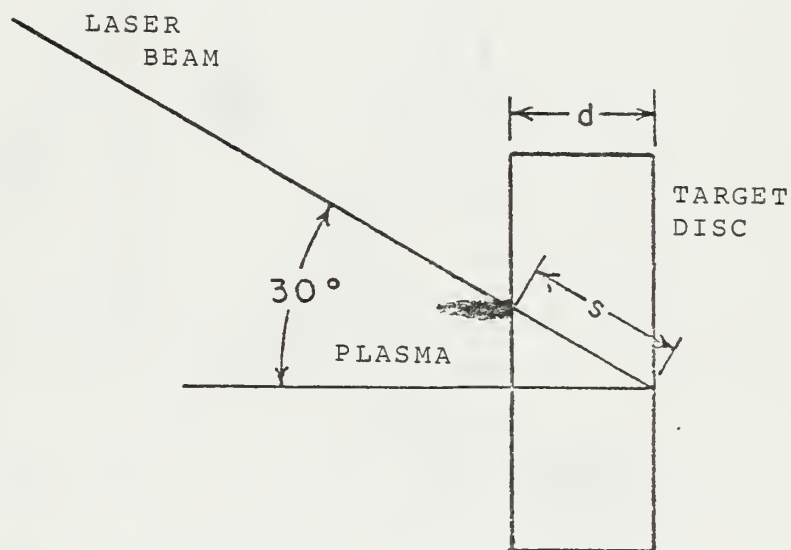


FIGURE 3. LASER TARGET IMPACT ANGLE



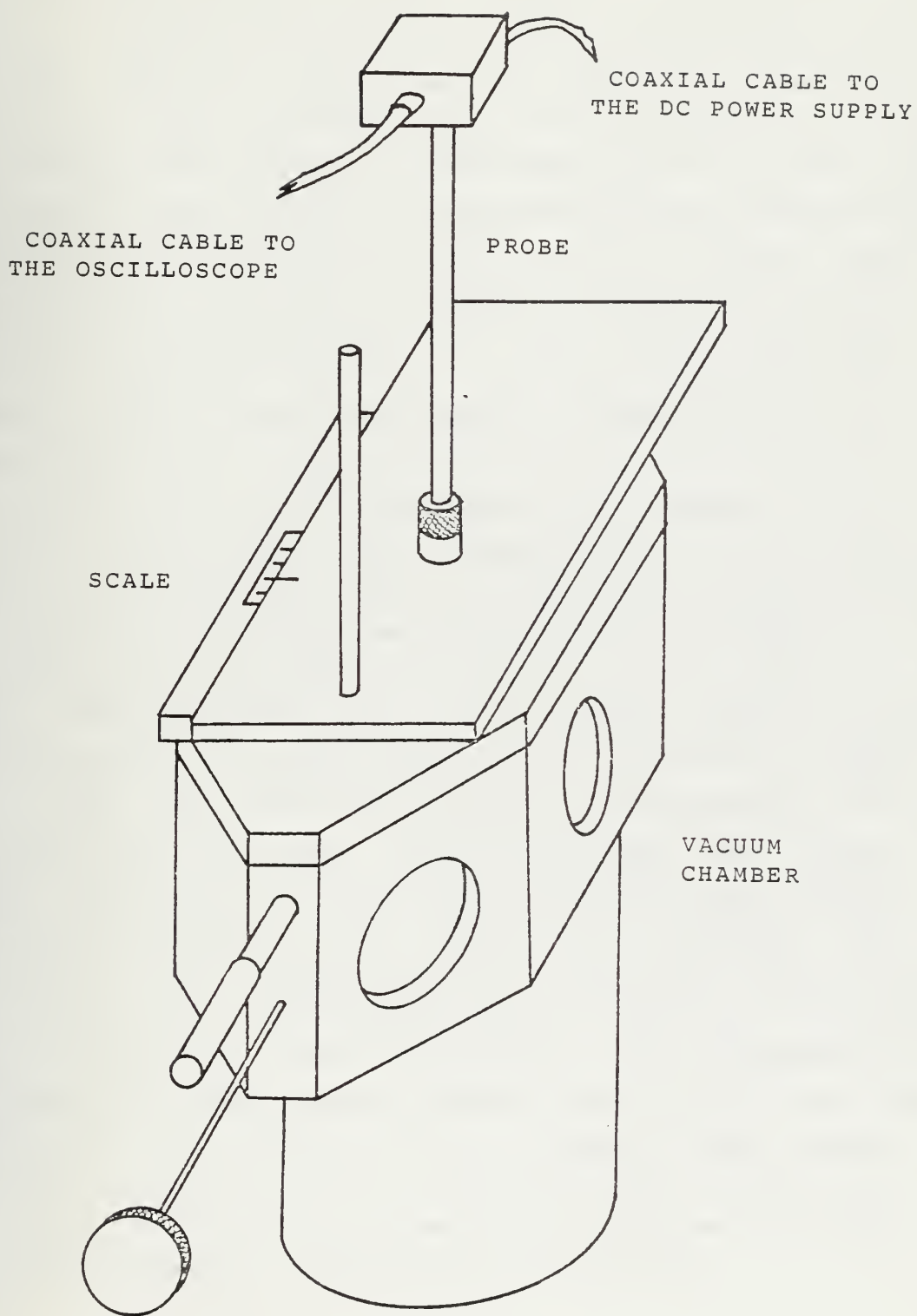


FIGURE 4. THE PROBE DISTANCE SCALE





The power supply used for the electrostatic probe circuit (see Appendix B for probe construction, theory and circuit design) was a Hewlett Packard 6218A power supply with a maximum voltage of 50 volts and maximum current of 200 mA. Early in the research using the electrostatic probe, it was determined that it was desirable to compare the signal peak values for different values of probe bias. A relative number equal to the measured peak voltage divided by the bias voltage could then be used for data reduction and graphing. The probe response, as graphed by Brooks [10] in previous research using the same probe, indicated the region from -10 volts to -20 volts DC bias to have the linear characteristics desired for accurate comparisons (see Figure 5.).

The points on this graph were an average of several hundred laser data shots, especially at -15 volts and -20 volts. The standard deviation of the main plasma peak value for those bias voltages was about 4 volts in each case. The average values did match up to Brooks' [10] graph of the same characteristics but no mention was made by Brooks of the accuracy of the data used to plot the curve in Figure 5.

When the probe bias voltage was determined, the data pictures could be taken. Five oscilloscope time scales (x axis) were used to take the data from the probe circuit, 20 nsec/cm, 50 nsec/cm, 100 nsec/cm, 200 nsec/cm, and 500 nsec/cm. Four voltage scales (y axis) were used to record the probe signal, 500 millivolts/cm, 1 volt/cm, 2 volts/cm, and 5 volts/cm. The 20 nsec/cm and 50 nsec/cm scales displayed the early plasma signals; that is, the fast moving particles that arrived prior to the main plasma pulse. The 100 and 200 nsec/cm scales showed the main plasma pulse and the 500 nsec/cm scale showed the late plasma signals, i.e. the particles with slow expansion velocities.



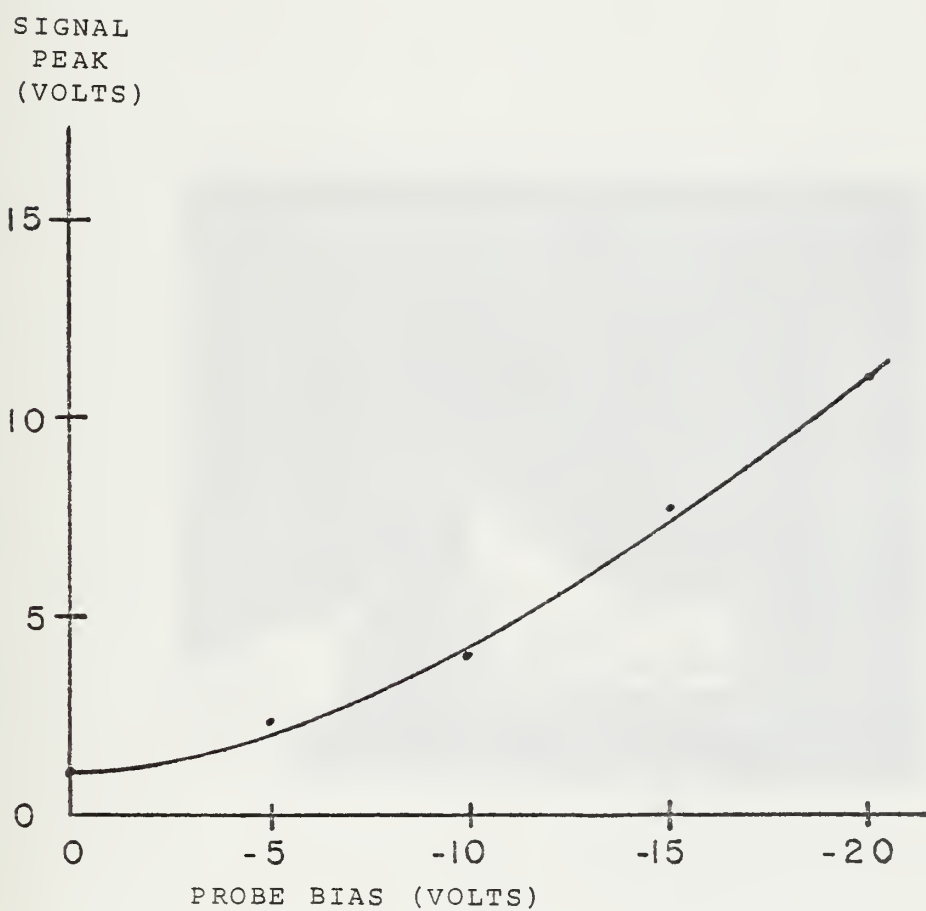


FIGURE 5. THE PROBE RESPONSE WITH THE PROBE 2 CM FROM THE TARGET SURFACE



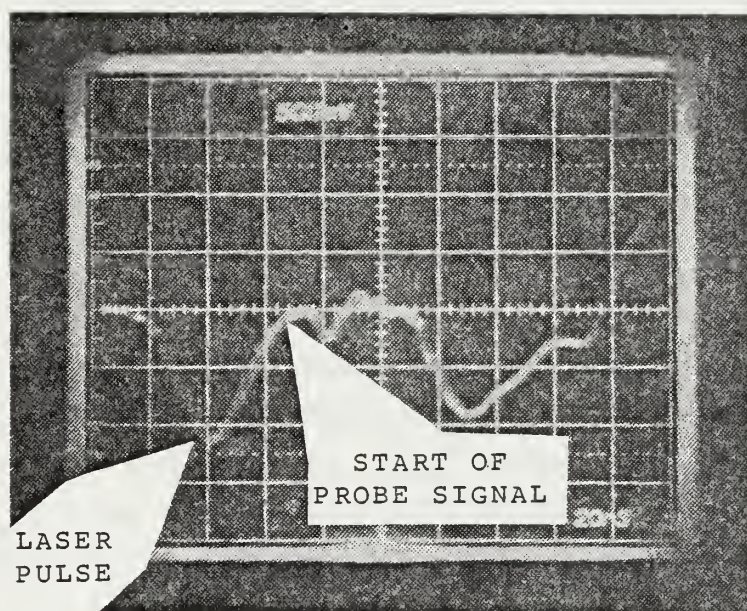


FIGURE 6. DATA PHOTO USING A 62 NSEC TIME DELAY CABLE



To be able to consistently record the signals in the same time reference, a zero time mark,  $t_0$ , had to be displayed on each photograph. The inverted laser pulse signal was used for the time reference. Initially, a long time delay cable (62 nsec and 48 nsec cables were used) was added to the probe circuit so that the probe signal followed the laser pulse signal by the time length of the delay cable. This technique worked very well for the early signals (20 nsec/cm time scale) but was found to add little to the larger oscilloscope time scale selections. On a 50 nsec/cm scale the delay cable only delayed the signal one cm and when a 500 nsec/cm scale was selected, the 0.1 cm delay on the oscilloscope graph was not even discernable. Eventually, the following techniques for timing were established as the method of extracting data from each time scale.

(1) The 20 nsec/cm time scale was easily read to 4 nsec. The laser pulse covers about 50 nsec from start to finish, so 48 nsec and 62 nsec delay lines were used and zero time for the plasma signal was assumed to be at 50 nsec or 60 nsec respectively. Measurements were made starting 2.5 or 3 cm from the edge of the graph (Figure 6.). This scale can read all probe signal peaks to about 80 nsec.

(2) For the 50 nsec/cm time scale, the best accuracy of measurement was 10 nsec. Since the 20 nsec/cm scale could read the signals to about 80 nsec, the 50 nsec/cm time scale was used for signals from 80 to 500 nsec. For this scale and all higher time scales, the time delay cable was removed and a replacement cable was used to match the trigger pulse up with the probe signal (see Figure 1). The peak of the pulse signals was used as the reference time  $t_0$  where,





$$t_0 = 40 + 5 = 45 \text{ nsec.}$$

All of the time values were measured from  $t_0$ , adding 45 nsec to get the actual time of the peak signal. For example, suppose a probe signal peak was 115 nsec from the laser pulse peak,

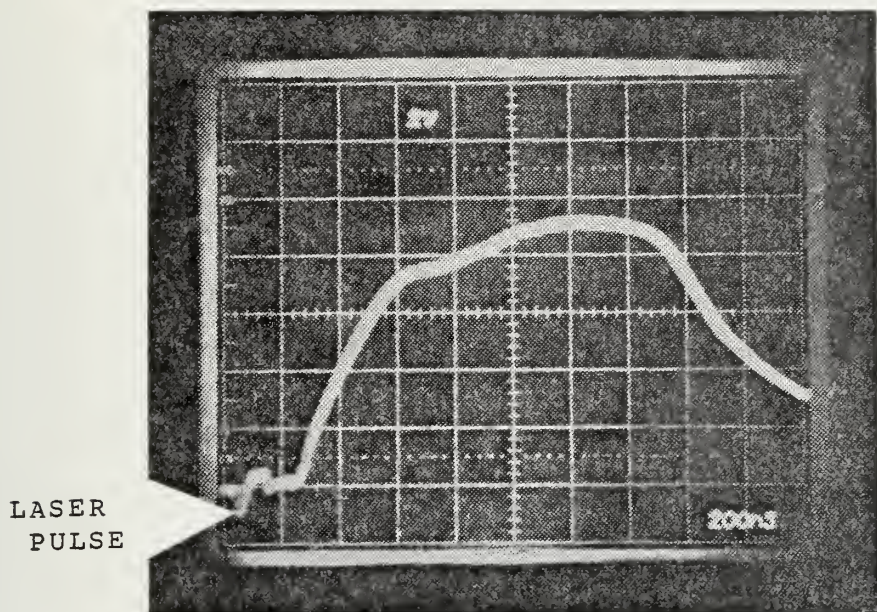
$$\begin{aligned} t_{\text{peak}} &= t + t_0 = 115 + 45 \\ &= 150 \text{ nsec.} \end{aligned}$$

(3) The 100 nsec/cm scale could be read with 20 nsec accuracy. The data from the 100 nsec/cm time scale was read like the 50 nsec/cm scale. The 100 nsec/cm time scale was used for peaks located from about 150 to 800 nsec.

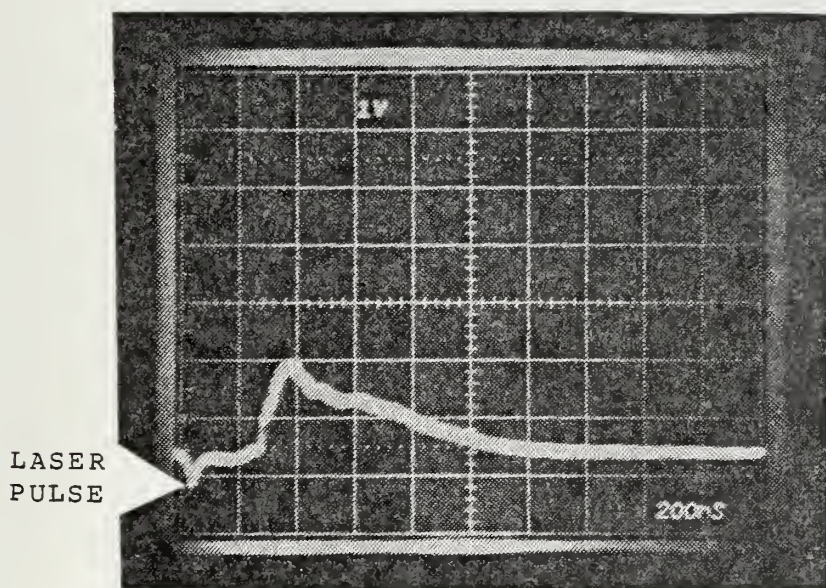
(4) The 200 nsec/cm scale could be read with 40 nsec accuracy. Now even the  $t_0$  value determined in (2) above is becoming insignificant. However, because of the ease of locating the peak of the laser pulse, the same method was used to determine time relationships (see Figure 7). The 200 nsec/cm scale could be used for signals from 200 nsec to about 1600 nsec.

(5) The 500 nsec/cm time scale was used to see if there were any very late signals. It could detect signals out to roughly 2,500 nsec. The time values accuracy for the 500 nsec/cm scale was 100 nsec. The  $t_0$  value was not significant to these figures and the time value of the peaks was read directly from the laser pulse peak (see Figure 8).





(a) DISTANCE FROM THE TARGET SURFACE TO THE PROBE EQUAL TO TWO CM

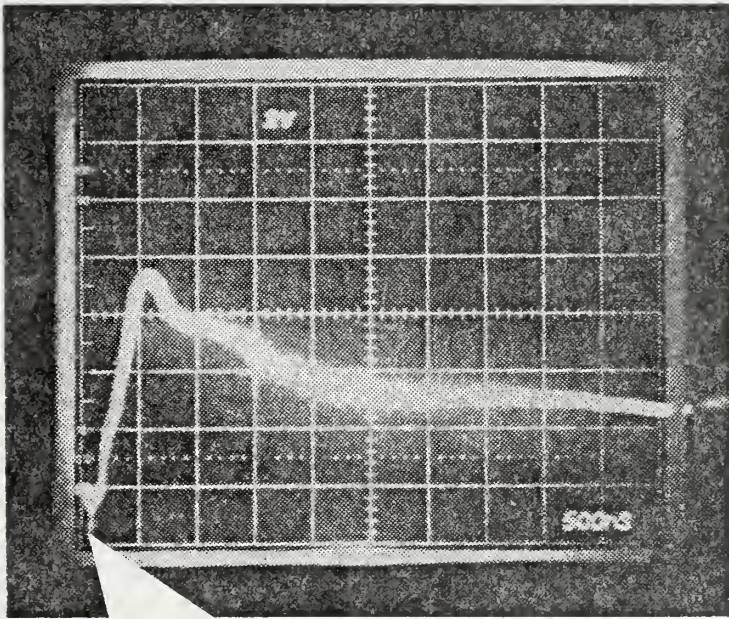


(b) DISTANCE FROM THE TARGET SURFACE TO THE PROBE EQUAL TO FIVE CM

FIGURE 7. TIME REFERENCE ON A 200 NSEC/CM TIME SCALE







LASER  
PULSE

FIGURE 8. THE PLASMA PROBE SIGNAL ON A 500 NSEC/CM SCALE





To take data from the graphs, a magnifying glass and Plexiglas certimeter grid scale were used. The magnifying glass facilitated more accurate readings of the plastic scale which could be lined up with the time reference point more readily. It also helped to reduce the eye strain pursuant to reading the graphical data.

The plasma probe signal occasionally had a high frequency noise signal superimposed on the laser pulse signal (see Figure 9). The noise signal only appeared during the time of the laser pulse. To determine what the signal was, the frequency was approximated as follows. From a 20 nsec/cm data shot, two oscillations were measured to be 0.4 cm long. That indicates the time constant,  $t_s$ , to be approximately 4 nsec. The frequency then is,

$$\begin{aligned} f &= 1/t_s = 1/4 \times 10^{-9} \\ &= 2.5 \times 10^8 \text{ cycles/sec.} \end{aligned}$$

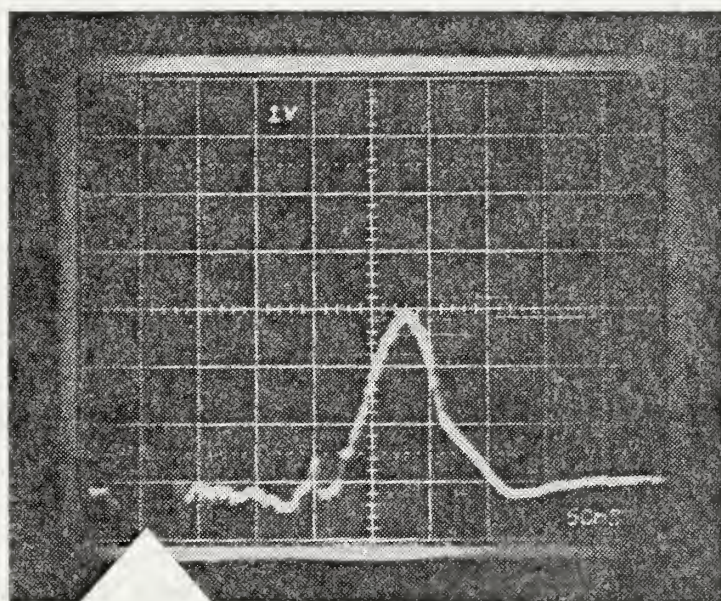
Unwanted electrical grounds were first suspected. Morrison [35] was consulted for grounding problems, but all were discounted. It was first thought that the noise was the electromagnetic field radiation from the Pockels cell being picked up by the MgO photodiode detector (K-D1). The detector fed the laser pulse signal to the oscilloscope. The noise seemed to be on the laser pulse signal. Introducing a long time delay line (62 nsec) or the electrostatic probe signal separated the noise from the laser pulse so the noise had to be coming from the probe. It was then conjectured that the probe was acting as an antenna receiving a signal from the Pockels cell, but that too was discounted because the signal disappeared when the probe was pulled up away from the target. No signal was received when the laser was fired with the probe in that



position, which contradicted the hypothesis that the probe was an antenna. Further investigation, to see how the noise signal changed as the laser burned a deeper hole into the target, indicated that the noise signals had something to do with the laser target interaction. For the first fifteen shots the noise signal was consistently present. As the laser hole got deeper, the signal disappeared. After the 15th shot, the signal rarely appeared and after the 40th shot on a single target spot, there was never a noise signal. Also, from a highly polished aluminum target surface (almost mirror quality), the noise signal was even more marked than from a dull surface. The conclusion was that the noise signal was due to either X-ray emission from the laser-target interaction or some sort of diffuse reflection (twinkle) from the target surface. To minimize the noise, the target surface was "cleaned" with an unfocused laser shot before each data run. The cleaning reduced the persistence of the high frequency noise signal but it did not totally remove it.

The data collected from each photograph were tabled for data reduction calculations (see Appendix C). For each picture, a unique 10 digit number was assigned to identify it. The shot number per target spot,  $N_s$ , on which the picture was taken was recorded. The distance of the probe from the target surface and the probe bias voltage were recorded. On some pictures, as many as three peaks could be distinguished. The time and voltage of each signal peak was recorded. The laser energy was recorded and the error of measurement of the peak times and peak voltages were recorded.





HIGH  
FREQUENCY  
NOISE

FIGURE 9. THE HIGH FREQUENCY NOISE SIGNAL SUPERIMPOSED ON THE LASER PULSE SIGNAL





A linear time to distance relationship was assumed and calculations were made on the basis of this assumption, i.e.  $d = vt$ . The velocities agreed with previous work at the approximate distance of the probe from the target surface (1 to 5 cm). McKee [44] determined the plasma velocity to be  $10^7$  cm/sec and Brooks [10] found laser produced plasma velocities of  $5.9 \times 10^7$  and  $1.1 \times 10^8$  cm/sec. Demtröder and Jantz [17] measured velocities of  $10^7$  cm/sec at 170 cm and Wei, Nelson, and Hall [59] measured velocities of  $10^6$  cm/sec at 4 mm so the linear velocity assumption was a valid one for the region 1 cm to 5 cm from the aluminum target surface.

The equation used to calculate the velocity,  $v$ , from the probe signal data was  $v = d/t$ , where  $d$  is the distance the plasma had to travel and  $t$  is the time of the plasma probe peak. A velocity was calculated for each probe signal peak. The distance,  $d$ , was assumed to equal the distance from the surface of the aluminum target to the probe,  $d_1$ , plus the distance from the bottom of the hole to the surface of the target,  $d_2$ , where  $d_2 = 0.01 N_s$  [cm] because each shot removed 0.01 cm of the target surface in the crater. If  $d_2$  were not taken into account, the deep holes ( $N_s \geq 40$ ) would have large measurement errors before the data reduction calculations are even begun.

Error analysis of the photographic data calculations of velocity and distance was also necessary to insure that the measured quantities were dependable. A simple scheme for error analysis found in reference [3] was used. The measurement errors for distance  $d$  were  $\delta d = \pm 0.05$  cm.





The time errors, dependent on which oscilloscope time scale was used, were:

Table 4. Oscilloscope Time Measurement Errors

SCALE	TIME ERROR ( $\delta t$ )
20 nsec/cm	$\pm 2$ nsec
50 nsec/cm	$\pm 5$ nsec
100 nsec/cm	$\pm 10$ nsec
200 nsec/cm	$\pm 20$ nsec
500 nsec/cm	$\pm 50$ nsec

The velocity calculation error was  $\delta v$ . The velocity formula was  $v = \bar{d}/t$ , so

$$\begin{aligned}\delta v &= \left| \partial v / \partial d \right| \delta d + \left| \partial v / \partial t \right| \delta t \\ &= \left| 1/t \right| \delta d + \left| -d/t^2 \right| \delta t\end{aligned}$$

A sample calculation of the velocity error for velocities of the order of  $2 \times 10^6$  cm/sec, with  $t = 500$  nsec,  $\bar{d} = 1$  cm,

$\delta t = 50$  nsec, and  $\delta d = 0.05$  cm gives:

$$\begin{aligned}\delta v &= (1/500) (0.05) + (1/(500 \times 10^{-9})^2) (50 \times 10^{-9}) \\ &= 10^5 + 2 \times 10^5 \\ &= 3 \times 10^5 \text{ cm/sec.}\end{aligned}$$



Table 5. Results of Velocity Error Calculations

$v$ [cm/sec]	$t$	$d$ [cm]	$\delta t$	$\delta d$ [cm]	$\delta v$ [cm/sec]	$\delta v/v$
$2 \times 10^6$	500 nsec	1	50 nsec	0.05	$3.0 \times 10^5$	15%
$6 \times 10^6$	330 nsec	2	10 nsec	0.05	$3.3 \times 10^5$	5.5%
$5 \times 10^7$	100 nsec	5	5 nsec	0.05	$3.0 \times 10^6$	6%

So the measurement errors of the velocities were not very important from a statistical point of view. For data analysis, errors of up to 30% were accepted as good data. The total number of velocity data points was reduced from 585, the number of peaks on the data photos, to 171, the number that ultimately survived the error analysis gate.



## V. RESULTS

The experimental results of the research completed for this thesis are presented in this section. Each aspect of the results has been subdivided into a subsection for easy identification. The results of this thesis were extracted from graphs obtained from computer analysis of the data. Four plasma ion velocities were found consistently in each shot series;  $4.0 \times 10^6$  cm/sec,  $5.6 \times 10^6$  cm/sec (the bulk of the plasma),  $1.5 \times 10^7$  cm/sec, and  $3.7 \times 10^7$  cm/sec, and a fifth,  $10^8$  cm/sec, appeared in a limited number of the data runs.

### A. CRATER DIMENSIONS

The crater dimensions were taken from two craters for measurements to approximate the amount of target material removed by each laser shot. The results were tabled in Table 3 and a graphical representation of the crater is shown in Figure 2. The deep crater had a cylindrical diameter of 0.11 cm. Each shot removed approximately 0.10 cm of target material. The surface hole of the crater differed in dimensions slightly from the deep, cylindrical shaped hole. It had a diameter of 0.17 cm. The difference was probably due to the surface boundary at the top of the crater only being bonded to the target on one side while the deep crater material had target material on three sides which reduced the erosion at the edges of the target spot.



## B. PROBE SIGNAL CHANGE ASSOCIATED WITH THE FIFTEENTH LASER SHOT

There seemed to be a consistent probe signal difference associated with about the fifteenth laser shot number that changed the laser plasma characteristics when the laser-target interaction angle was  $30^\circ$ . It was detected in this research with an electrostatic probe, Shewchuk [49] detected it with X-ray photodiodes, and Williamsor [61] detected it with magnetic probes.

To explain this anomaly it was speculated that the  $30^\circ$  laser beam incidence angle was hiding the incidence impact area from the probes after the fifteenth shot. A quick calculation using the laser cratering statistics of Table 3 showed that by approximately the fifteenth shot the impact area is hidden. Additional support to this hypothesis was lent by Shewchuk's research. With the X-ray probes in a position normal to the target surface, the X-ray signal began to get weak after the fifteenth shot. One X-ray probe was continually collecting a greater signal strength than the other. When the probes were positioned nearly parallel to the laser beam so that they could nearly look directly down the crater there was no signal change no matter how many shots were taken on a single crater. The consistent X-ray signal indicated that there was no special significance to the fifteenth laser pulse other than the mechanical blocking of the signal by the crater edge.





### C. PLASMA ELECTRON TEMPERATURE

Electron plasma temperature can be found from the slope of the electrostatic probe characteristics (see Figure 5) at the graphical origin, (0,0), using an equation for electrostatic probe diagnostics from Chen [25].

$$\begin{aligned} dI/dV &= (e/kT_e) (i_{1+} i_{2+}) / (i_{1+} + i_{2+}) \\ &= ei/2kT_e \end{aligned}$$

where  $i = i_{1+} = i_{2+}$  because the double probe used was symmetric. The measured value of  $dI/dV$ ;

$$dI/dV = 1.5/5 = 0.3 \text{ amps/volt}$$

by extrapolation of the graph in Figure 5 and comparison with Brocks' graph [10] of the same data. The value of  $i$  is  $i = RV_s$  where  $V_s$ , the probe saturation voltage, is equal to 30 volts and  $R_s$ , the signal resistance, is equal to 1 ohm.

$$\begin{aligned} T_e &= (ei/2k) (dI/dV)^{-1} \\ &= (11609/2) 30 (0.3)^{-1} \\ &= 58 \times 10^4 \text{ } ^\circ\text{K} \\ &= 48 \text{ eV.} \end{aligned}$$

So, the plasma electron temperature is approximately 50 eV two cm from the target surface.



## D. PLASMA DENSITY RESULTS

The plasma density,  $n_i$  [ $\text{cm}^{-3}$ ], for each characteristic plasma velocity is derived in Appendix B from the equation:

$$n_i = \frac{I}{Ze(1+s)} \frac{A}{p} \frac{V}{I_P}.$$

Appendix B defines all of the terms of the equation and makes the necessary approximations to arrive at the density for each probe signal velocity (see Figure 13). The analytic correspondences of velocity to density were found to be;  $4.00 \times 10^6$  cm/sec to  $4.09 \times 10^{13}$   $\text{cm}^{-3}$ ,  $5.57 \times 10^6$  cm/sec to  $7.34 \times 10^{13}$   $\text{cm}^{-3}$ ,  $1.52 \times 10^7$  cm/sec to  $10^{13}$   $\text{cm}^{-3}$ ,  $3.71 \times 10^7$  cm/sec to  $1.03 \times 10^{12}$   $\text{cm}^{-3}$ , and  $1.01 \times 10^8$  cm/sec to  $1.08 \times 10^{11}$   $\text{cm}^{-3}$ .



## E. VELOCITY DISTRIBUTION ANALYSIS OF THE PROBE SIGNALS

The velocity distribution of the plasma particles is an important consideration in containment schemes for plasmas. The container wall interaction with the plasma can be predicted if a velocity distribution model for the plasma is accurate. The point of this section is to analyse the probe temporal signals for velocity distribution.

In order to deduce velocity distributions from the probe current, the time function must be analyzed. If the particle velocity is given by  $v = d/t$ , then  $v^2$  is proportional to  $1/t^2$ . The one dimensional Maxwellian velocity distribution is:

$$dN/dv_x = f_v(v_x) = N(1/v_m \{ \pi \}^{1/2}) \exp(-v_x^2/v_m^2)$$

where  $v_m = (2kT/m)^{1/2}$

$N$  = number of particles  
 $k$  = Boltzmann's constant  
 $T$  = plasma temperature  
 $m$  = particle mass.

A Gaussian time distribution,  $f(t)$ , is of the form:

$$f(t) = A_0 \exp(-(t-t_0)^2/2s^2)$$

where  $A_0$  = the peak value

$t_0$  = value of  $t$  at the peak

and  $s$  = standard deviation.



SIGNAL GRAPHED IN  
FIGURE 11

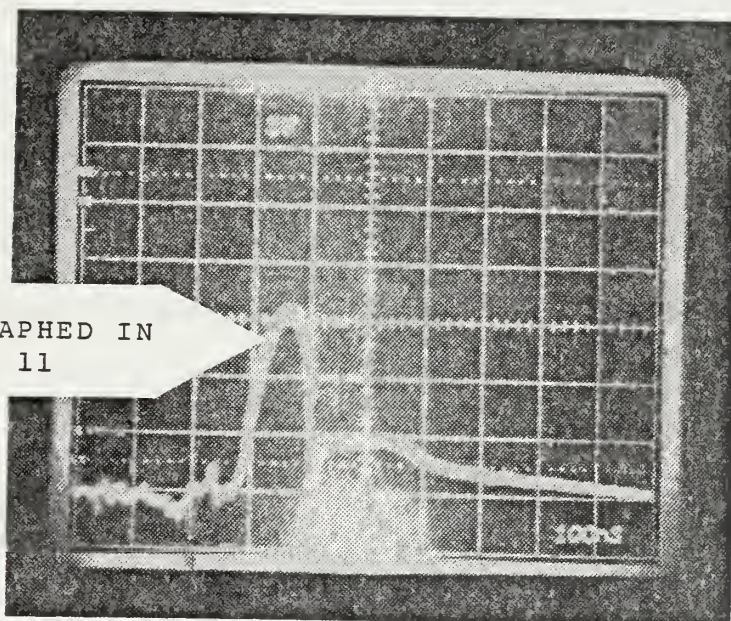


FIGURE 10. DATA PHOTO FOR GRAPH OF ION VELOCITY DISTRIBUTION





The standard deviation is a parameter which controls the relative flatness of the bell shaped curve. A small value for  $s$  results in a sharp peak and a large value of  $s$  results in a broad, flat shape.

Now if all particles of a velocity group are considered to start from a single point at one time, with the Maxwell Boltzmann distribution of velocities in one direction, then the distribution of the particles with respect to arrival times at the probe can be deduced as,

$$dN/dt = (dN/dv_x) (dv_x/dt),$$

and since  $v_x$  is related to the arrival time through the relationship  $v_x = d/t$ , then

$$dv_x/dt = -d/t^2,$$

$$\begin{aligned} \text{and} \quad dN/dt &= \{N(\pi v_m^2)^{-1/2} \exp[-(d/t)^2 / v_m^2]\} (-d/t^2) \\ &= (\text{constant}) t^{-2} \exp[-(d/t)^2 / v_m^2]. \end{aligned}$$

This formula does not analytically approximate the Gaussian form in any apparent limit. In the course of this research the probe response signals, however, appeared to approach a Gaussian form (see Figure 10). Further graphical analysis of the data photos indicated that velocities taken from the probe signals reasonably fit Gaussian curves. In Figure 11, the data from the photo in Figure 10 was graphed and fitted to a Gaussian curve (A-B) successfully. Curve A was the actual curve from the photo. In Figure 11 the results of subtracting out the particles with velocities that belonged to the next peak (curve B) made the Gaussian fit even better. For the curve A-B the Gaussian fit equation was:



$$f(t) = 2.53 \exp(-\{t-150\}^2 / 4419)$$

and for curve E:

$$f(t) = 3.10 \exp(-\{t-160\}^2 / 3804).$$

Further analysis to explain these unexpected results is required.



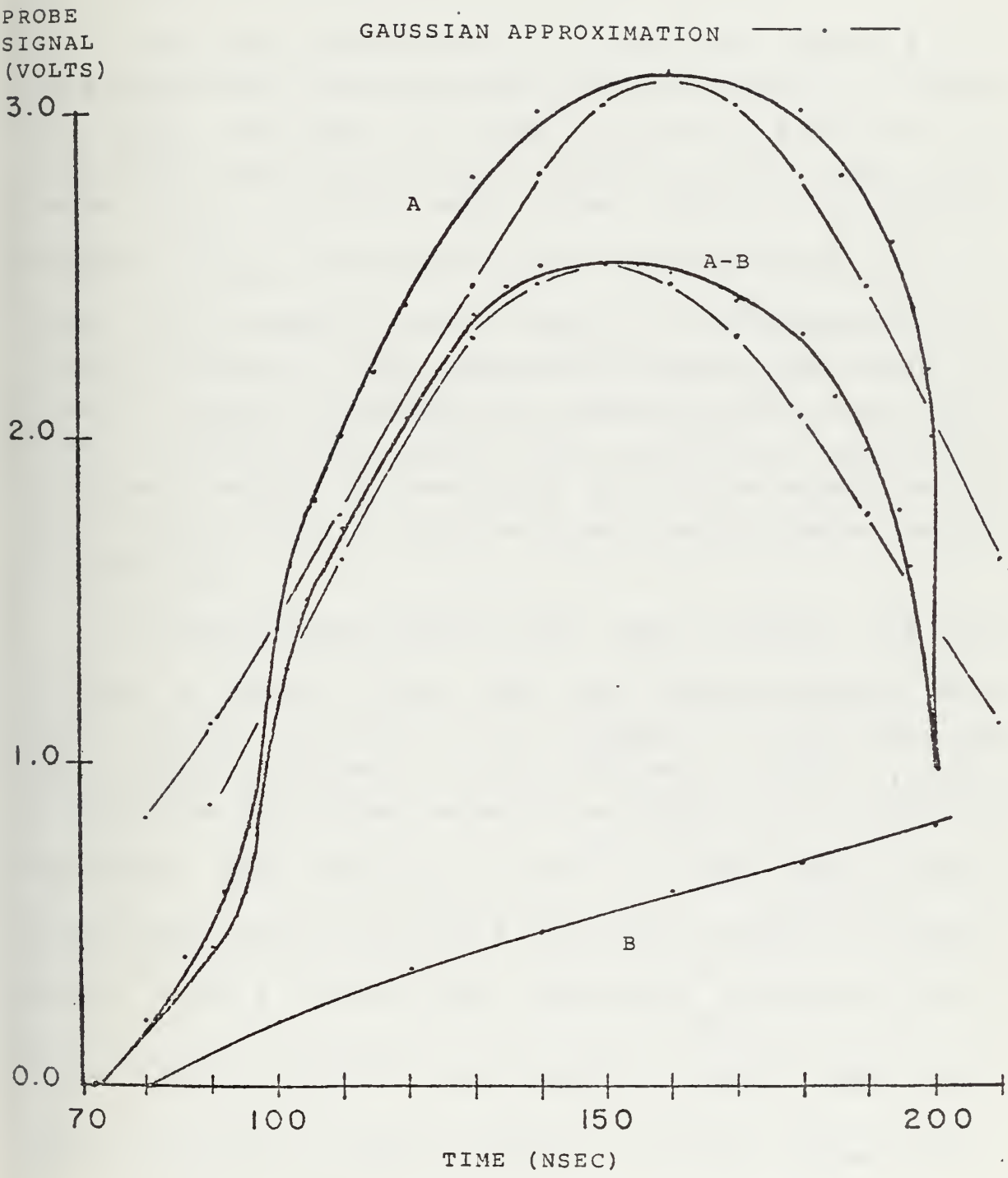


FIGURE 11. GRAPH OF AN ION VELOCITY DISTRIBUTION





## F. PLASMA PARTICLE VELOCITY GRAPHICAL RESULTS

The total picture of all of the plasma velocity data with measurement errors less than 30% was graphed in Figure 12. Each data peak was used to calculate a velocity and each signal peak value,  $V$ , was divided by the DC probe bias value,  $V_{IC}$ , to state each signal value as a unitless fraction,  $V/V_{IC}$ , for inclusion of a range of values for  $V_{DC}$ . There is a marked visual effect of the distribution of points in Figure 12 that immediately suggests that there are several discrete characteristic plasma particle velocities. Figure 13 carries the analysis one step further, showing the graphical results of averaging all of the velocities and peak values in groups around each particularly dense region in Figure 12.

The slow signals (less than  $5 \times 10^6$  cm/sec) did not survive as valid points when the maximum allowable data error was 30%. If the error was allowed to be 50% then the slow signals remained in the analysis. That is what produced the slow signal velocity in Figure 13. Particle velocities were found to be  $4.0 \times 10^6 \pm 1.2 \times 10^6$  cm/sec with a signal peak value ( $V/V_{DC}$ ) of  $0.21 \pm 0.10$ ;  $5.6 \times 10^6 \pm 0.25 \times 10^6$  cm/sec with a signal peak value ( $V/V_{DC}$ ) equal to  $0.50 \pm 0.13$ ;  $1.5 \times 10^7 \pm 0.26 \times 10^7$  cm/sec with a signal peak value equal to  $0.19 \pm 0.08$ ;  $3.7 \times 10^7 \pm 0.76 \times 10^7$  cm/sec with a signal peak value equal to  $0.05 \pm 0.04$  and  $1.0 \times 10^8 \pm 0.5 \times 10^8$  cm/sec.



cm/sec with a signal peak value equal to  $0.03 \pm 0.03$ . The very fast ( $1.0 \times 10^8$  cm/sec) plasma velocity was taken from a data sample of only three points out of 171 data points. Even though the error bars for that data in Figure 13 are small, the probable error is not, due to the paucity of data points.

In Appendix B the ion density,  $n_i$ , was tabled as a function of the plasma particle velocities,  $v_{LF}$ . The Boltzmann equation is:

$$r(E) = n_0 e^{-E/kT}.$$

If  $E = mv^2/2$

then  $n = n_0 \exp(-\{mv^2/2kT\})$

$$= n_0 \exp(-v^2/v_m^2)$$

where  $v_m^2 = m/2kT.$



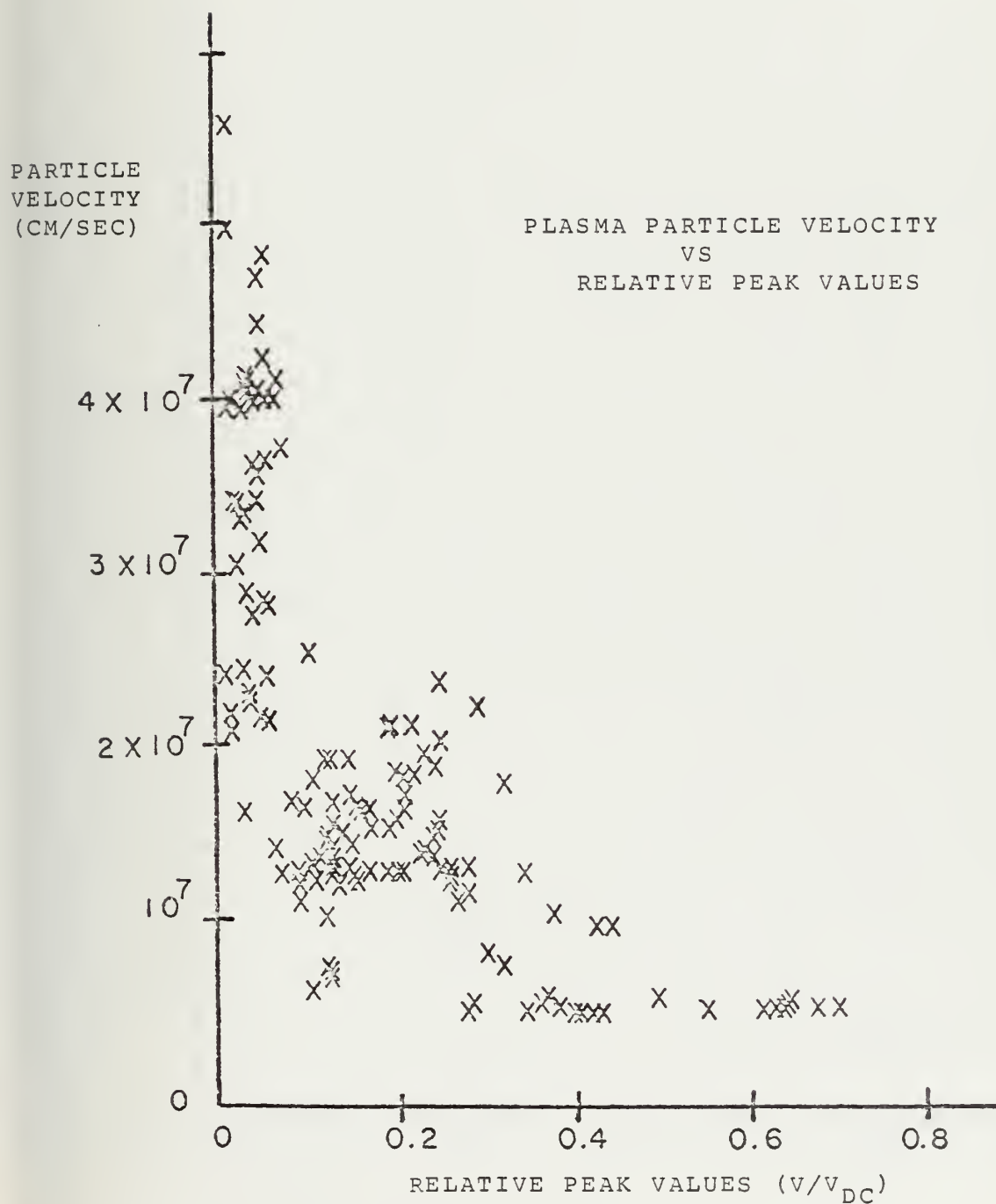


FIGURE 12. GRAPH OF COMPUTER ANALYSIS RESULTS



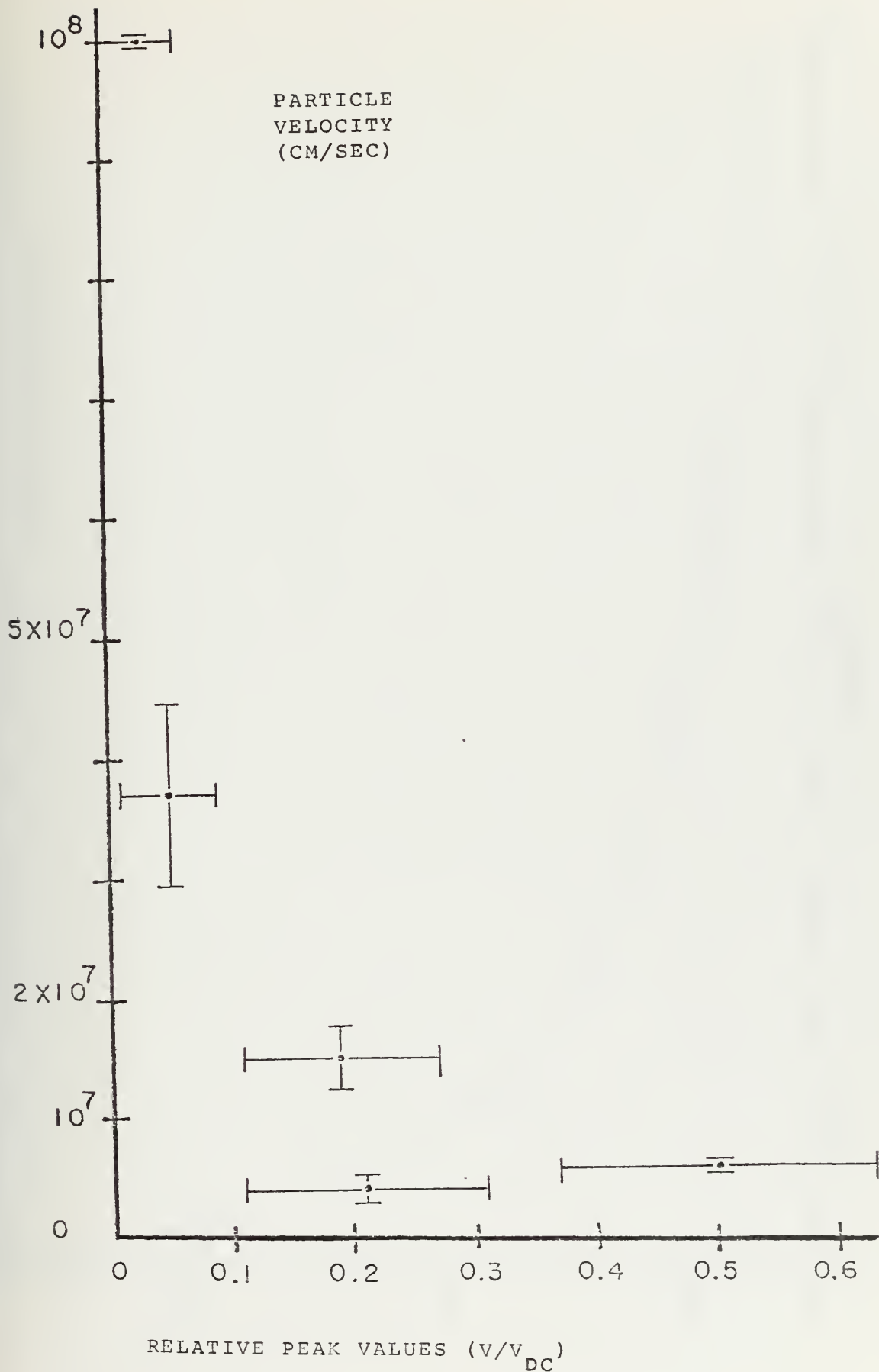


FIGURE 13. GRAPH OF THE PLASMA VELOCITIES





GRAPH OF  $\ln(n)$  VS  $v^2$

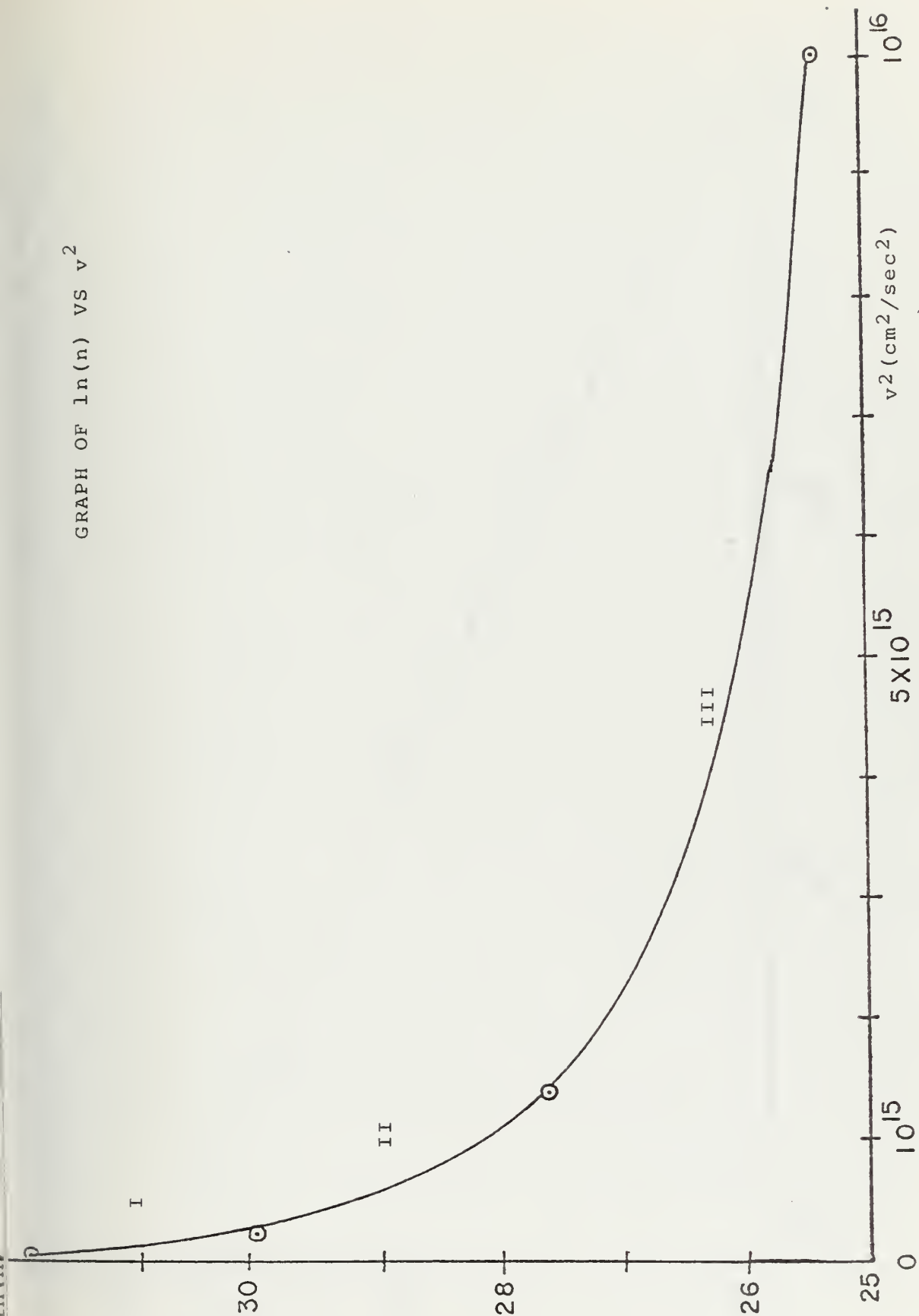


FIGURE 14. GRAPH OF  $\ln(n_i)$  VERSUS  $v^2$



GRAPH OF  $\ln(\ln(n))$  VS  $\ln(v^2)$   
 NOTE THAT THE SCALES ARE LOGRITHMIC

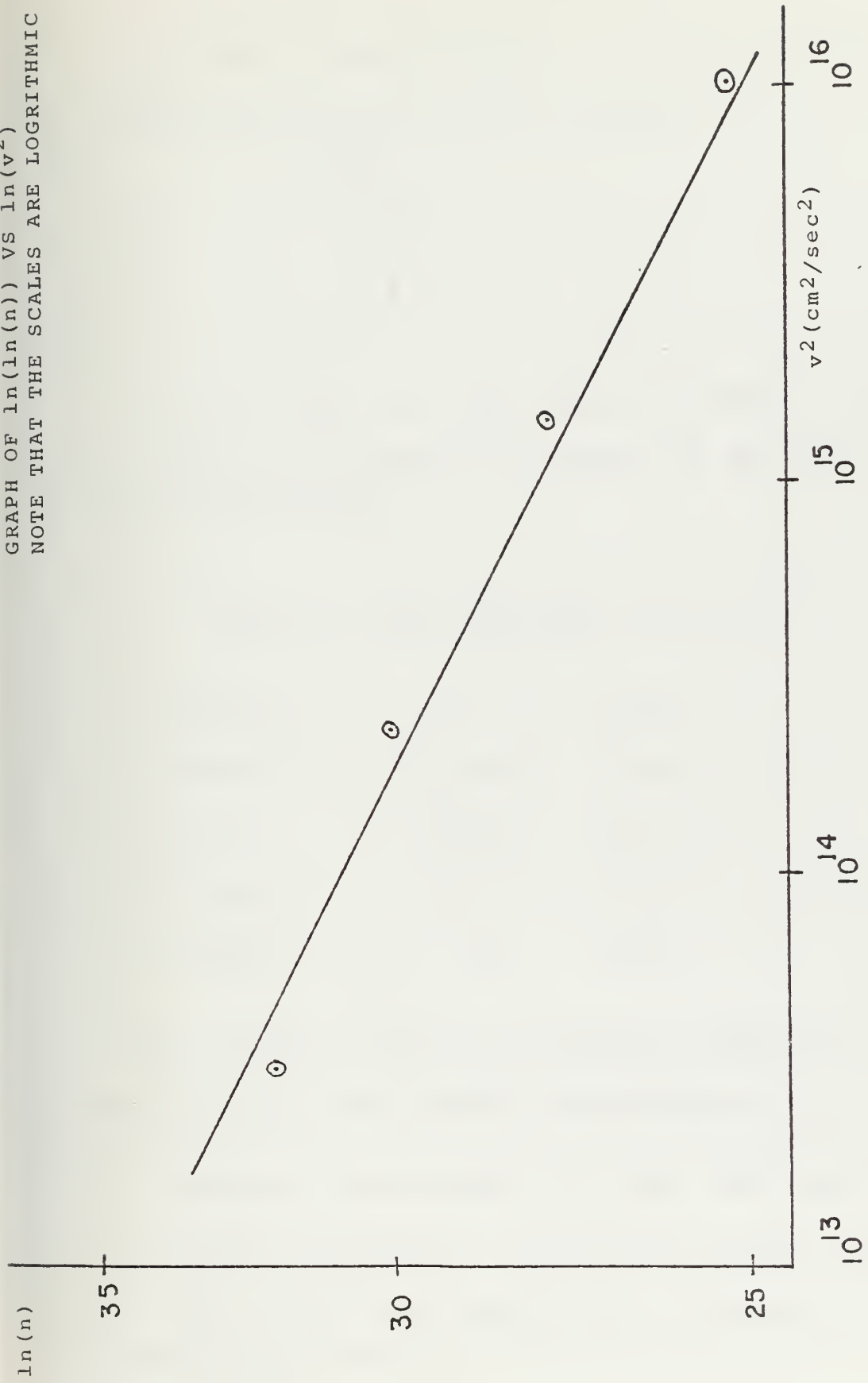


FIGURE 15. GRAPH OF  $\ln(\ln(n))$  VERSUS  $\ln(v^2)$



$$\text{So, } \ln(n) = \ln(n_0) - (v^2 / v_m^2)$$

or a linear equation of the form  $y = ax + b$

$$\begin{aligned} \text{where } y &= \ln(n) \\ b &= \ln(n_0) \end{aligned}$$

$$a = -1/v_m^2$$

$$\text{and } x = v^2.$$

If the graph of  $\ln(n)$  versus  $v^2$  yields a straight line then the set of points in Figures 12 and 13 fit a Ecltzmnn distribution.

Table 6. Data Points for  $\ln(n)$  vs.  $v^2$

$v$ [cm/sec]	$v^2$	$\ln(n)$
$5.57 \times 10^6$	$3.1 \times 10^{13}$	31.93
$1.52 \times 10^7$	$2.3 \times 10^{14}$	29.93
$3.71 \times 10^7$	$1.4 \times 10^{15}$	27.66
$1.01 \times 10^8$	$10^{16}$	25.41

The graph of  $\ln(n)$  vs  $v^2$ , shown in Figure 14 did not produce a straight line, so the relationship of  $n_i$  to  $v^2$  is not a Ecltzmnn distribution. A plot of  $\ln(\ln(r))$  vs  $\ln(v^2)$ , however, did produce a reasonably straight line (see Figure 15). So, the theoretical relationship is an exponential power relation.





If  $\ln(n) = c(v)^2^K$ , where  $c$  and  $K$  are constants.

So,  $\ln(\ln(n)) = \ln(c(v)^2^K) = \ln(c) + K\ln(v^2)$ , is

the graph of a straight line,  $y = ax+b$ , with  $y = \ln(\ln(n))$  and  $x = \ln(v^2)$ . The graph would then give a geometrical value for  $K$  equal to the slope (see Figure 15). If the slope is  $K$  not equal to 1, then the Boltzmann equation is not a solution.

The graph of  $\ln(\ln(n))$  versus  $\ln(v^2)$  is a straight line with slope equal to  $-3.86 \times 10^{-2}$ . So, the relationship between  $n$  and  $v$  is an exponential power relationship, not a Boltzmann distribution as postulated.

Error analysis indicates that the probable error in the  $y$  coordinate of Figure 15 is negligible and the error bars in the  $x$  direction (about 35%) are such, that if the data point is taken to be at either extreme, it is still on the line in Figure 15, indicating a very reliable power relationship between  $\ln(n)$  and  $v^2$ . Graphical analysis yields:

$$\ln(n) = c(v)^{2-0.0386}$$

and the number density is proportional to  $\exp(c(v)^{2-0.0386})$ .

On the assumption that all ions detected are aluminum, the kinetic energy differences between the characteristic velocity groups can be compared with the ionization energies of the multiply ionized states of aluminum (shown in Table 8). For example with  $v_2 = 1.52 \times 10^7$  cm/sec and  $v_1 = 5.6 \times 10^6$  cm/sec, two of the characteristic plasma particle velocities, the resultant energy difference for interval I in Figure 14 is:



$$E_2 - E_1 = (mv_2^2/2) - (mv_1^2/2)$$

where m is the mass of an aluminum atom,

$$m = 27(1.67 \times 10^{-24}) \text{ gm}$$

and 
$$v_2^2 - v_1^2 = 2 \times 10^{14} \text{ cm}^2/\text{sec}^2$$

so 
$$E_2 - E_1 = 4.53 \times 10^{-9} \text{ erg}$$
  

$$= 2.71 \text{ KeV.}$$

Similarly  $E_3 - E_2$  and  $E_4 - E_3$  were calculated for intervals II and III. For an aluminum mass  $E_3 - E_2 = 16 \text{ KeV}$  and  $E_4 - E_3 = 122.7 \text{ KeV}$ . If m is assumed to be a hydrogen mass, then  $E_3 - E_2 = 590 \text{ eV}$  and  $E_4 - E_3 = 4.54 \text{ KeV}$ . If the particles were assumed to be electrons  $E_4 - E_3 = 2.51 \text{ eV}$ .

The value of the change in kinetic energy resolved from these calculations is similar to the difference between the ionization energies of  $\text{Al}^{12+}, 13+$  and  $\text{Al}^{11+}$  ions. The ionization energies are listed here for comparison (all of the ionization energies are rounded to the nearest whole number).

Table 8. Aluminum Ionization Energies

$\text{Al}^+$	6 eV
$\text{Al}^{2+}$	19 eV
$\text{Al}^{3+}$	28 eV
$\text{Al}^{4+}$	120 eV



Al <sup>5+</sup>	154 eV
Al <sup>6+</sup>	190 eV
Al <sup>7+</sup>	240 eV
Al <sup>8+</sup>	285 eV
Al <sup>9+</sup>	330 eV
Al <sup>10+</sup>	400 eV
Al <sup>11+</sup>	440 eV
Al <sup>12+</sup>	2090 eV
Al <sup>13+</sup>	2300 eV

It is not clear why the velocities are grouped, but looking at the aluminum ionization energies, four groups can be readily approximated; Al<sup>+</sup> in group one, Al<sup>2+,3+</sup> in group two, Al<sup>4+-11+</sup> in group three, and Al<sup>12+,13+</sup> in group four.

If a local Boltzmann equilibrium is assumed to hold for each interval in Figure 14, then the kinetic energy of 2.7 KeV derived above can be equated to a temperature. This temperature does not correspond with the X-ray energy of several hundred electron volts detected by Shewchuk[49], but it does correspond very well to the Al<sup>+13</sup> ionization energy. The possibility exists that the velocity groups result from the degree of electron stripping. For example, Al<sup>12+,13+</sup> ions correspond to a signal velocity of  $10^8$  cm/sec, group three ions correspond to velocities of  $3.7 \times 10^7$  cm/sec, group two ions correspond to velocities of  $1.5 \times 10^7$  cm/sec and Al<sup>+</sup> ions correspond to  $5.6 \times 10^6$  cm/sec.



The target material should be changed from aluminum to some other metal element whose electron separation energies are also known. This would either lend further support to the group energy hypothesis or cause the hypothesis to be rejected. Further study of this phenomenon is required for a complete understanding of the theory.

#### G. OTHER VELOCITY RESULTS

There seems to be a mathematical pattern associated with the four plasma velocities. For convenience of notation let the characteristic plasma velocities be represented by:

$$a = 5.6 \times 10^6 \text{ cm/sec}$$

$$b = 1.5 \times 10^7 \text{ cm/sec}$$

$$c = 3.7 \times 10^7 \text{ cm/sec}$$

and  $d = 10^8 \text{ cm/sec}.$

Then, fractionally comparing each velocity to the velocity closest to it in magnitude with the faster velocity in the numerator and the slower velocity in the denominator, the relationships are:

$$c/c = 2.7$$

$$c/b = 2.5$$

$$b/a = 2.7.$$

This relationship is a noteworthy constant. Its applicability, however, is not apparent. Similarly, other velocity relationships are also geometrically ordered;

$$d/b = 6.7$$

$$c/a = 6.6$$





and

$$c/a = 18.$$

There is considerable implication that these number relations are significant. Their application to any theoretical development is not clear. A possible explanation may lie in the aluminum ionization energy groups discussed previously. Pursuit of this conjecture was not carried any farther in this thesis.

#### H. COMPOSITE PRCBE RESPONSE

The main plasma signal velocity and shape compared well with previous work. However, the early signals which were thoroughly investigated were neither consistent nor reproducible. Isercor [27] found that the early signals were strongly dependent on the surface conditions and the composition of the gaseous atmosphere inside of the vacuum chamber. Isenor was working in pressures from  $10^{-5}$  torr to  $10^{-3}$  torr. Porteus [41] found that at  $10^{-8}$  to  $10^{-9}$  torr there were no early signals. Porteus indicated that the impurities in the space inside of the vacuum chamber could be the cause of the early signals; vaporized oil from the diffusion pump, residual atmospheric air gases at the low concentrations inside of the vacuum chamber, aluminum vapor from previous laser shots, aluminum oxide vapor on the target surface, and even grease vapor from human handling of the target while putting it in the vacuum chamber and taking it out. All of these sources of contaminants tend to distort the probe signal from the aluminum plasma. Hydrogen, from a molecular layer of diffusion pump oil on the target surface, could also be the cause of the early signal.

From looking at many electrostatic probe pictures, an



average electrostatic probe response signal seemed to suggest itself (see Figure 16). The peaks got larger when the probe was closer to the target surface and grew smaller as the probe was moved farther away, indicating that the plasma spread out as it moved away from the target surface.



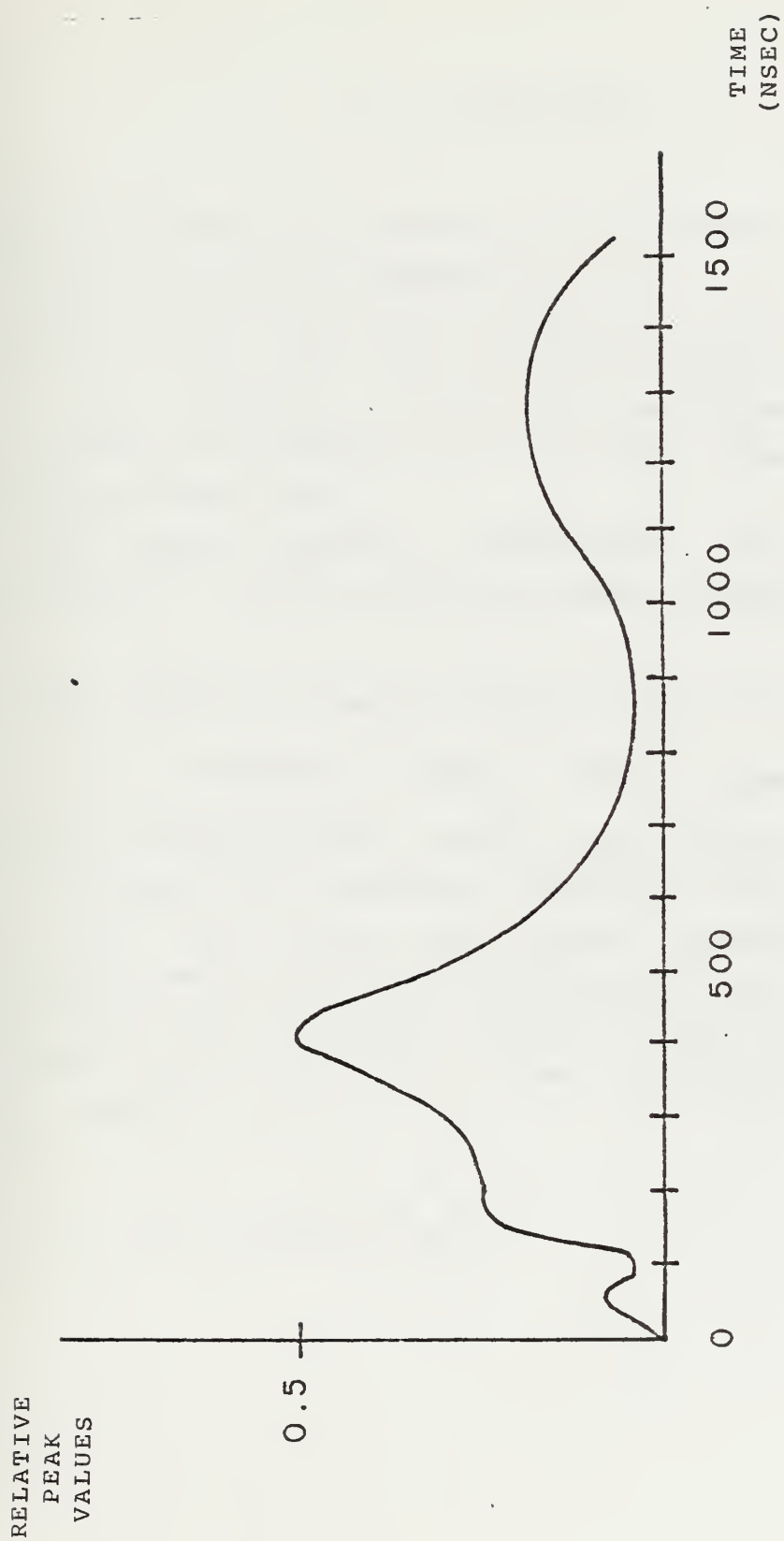


FIGURE 16. AVERAGE ELECTROSTATIC PROBE RESPONSE SIGNAL





## VI. CONCLUSIONS

In conclusion the results of the research represented by this thesis are to be summarized.

The laser-produced crater was made at the rate of 0.01 cm per laser shot. The crater cylinder diameter was 0.11 cm. At the fifteenth laser shot on a target crater, the impact surface was shielded from the probe when the laser incidence angle was 30°.

The plasma electron temperature was calculated analytically at two cm from the target surface to be about 50 eV.

The plasma ion density varied from  $10^{11}$  to  $7.34 \times 10^{13}$  cm<sup>-3</sup> for the streaming plasma. These densities were calculated from data using a double electrostatic probe.

Ion groups of different velocities were observed. Within the main group, the plasma particle velocity distributions were shown to be approximated by a Gaussian distribution. The ion number density in each velocity group was demonstrated to obey the Boltzmann equation for limited velocity ranges.

$$r(v) = n_0 \exp\left[-v^2 / v_m^2\right]$$



Relatively large temperatures were calculated using Eoltzmann approximations. An aluminum ionization energy theory was stated to offer an explanation, but more questions need to be answered before a conclusive argument can be offered.

Also, some interesting analytical ratios were produced by dividing each velocity by all the others. Uniform constants resulted which were not explained.



## VII. FURTHER RESEARCH

The areas warranting further study that arose during the course of experimentation are:

(1) Investigate the plasma velocities of laser-target interaction using electrostatic probes but with different target materials (metals). An increase in plasma ion mass should markedly reduce their velocities. If this is pursued for research, the laser-target interactions of the oxides of the target metals should also be investigated to resolve the question of how much the oxides contribute to the plasma pick signal.

(2) A concurrent project for further research is to use alternate plasma diagnostic techniques for examination of the laser produced plasma characteristics. Laser-plasma research at the Naval Postgraduate School has only been done using electrostatic probes, magnetic probes, pressure probes and X-ray photodiode probes. Curved capacitor energy analyzer probes, spectroscopic techniques and using a second laser shining through the plasma all offer very interesting alternatives for collecting the laser produced plasma characteristics data [45]. Huddleston and Leonard [25] and Swift [53] should be consulted as reference to begin research in this area.

(3) An investigation of the comments made by Forteus [41] and Isenor [27] about the relationship of background pressure to plasma ion velocity would make a good experimental series for thesis research.

(4) Research the fluid mechanics of the laser induced target crater formation. This is an area for some



good, thought provoking study. It would contribute some necessary and useful knowledge about the laser target interaction.

(5) Another project for someone who is interested in boundary value problems and is good at computer analysis would be to take one of the simple, analytically unsolvable plasma models such as the NRL models in reference [37], [38], and [39] and set it up for computer analysis. A good course to take if this project is undertaken is MA 3243, Numerical Methods for Partial Differential Equations, a core course in the Meteorology program. Reference texts by Smith [50], Ames [1], and Spiegel [51] would also assist research in this area.

(6) Another project, more of a systems nature, would be to investigate the systems aspect of having available a reasonable annual budget (\$50K) for plasma research. What direction should the spending proceed would be the hypothesis with an eye toward the Laser-Plasma Laboratory as a complete system including electrical power requirements, space availability, equipment advances, student population, and the total cost figures for the operation. If the Laser Plasma Laboratory at the Naval Postgraduate School is to continue to produce good results, the publicity from such a thesis would be a beneficial side effect. A good paper to start with for such a research project is reference [5]. A visit to laboratories at NWC China Lake, Berkeley, Livermore, and Sandia would also give a student of systems analysis a look at what state of the art research equipment is available.

(7) If the laser pulses are continued after a crater hole has passed all the way through the target, does the probe signal change? Investigation of this question would give a more complete understanding of the laser-target interaction.

(8) The statements made in this paper about the energy velocity groups possibly being associated with the





aluminum ionization should be investigated. If results of that sort can be derived using target material other than aluminum, the hypothesis would be supported by a more conclusive argument.

Also, the relationship of the velocity ratios needs further work. An explanation for the apparent geometric symmetry of the ratios was not discussed here. Further work with this theory should try to find a descriptive model to resolve it.

(9) The plasma velocity as a function of mass was attempted, but, due to time limitations, was not completed. There appear to be signals grouped at various velocities in Figure 12 and another possible explanation for the existence of the various velocity groups, besides the ionization theory, could be a mass theory. The slow signals may be produced by heavy atoms (AL, O) and the fast signals by light particles (E). The suggestions by Isenor [27] and Perceus [41] that chamber contaminants cause the large early-time peaks is further impetus to a theory dependent on particle masses.



## APPENDIX A

### THE LASER SYSTEM

The Naval Postgraduate School Laser-Plasma Laboratory Nd:glass laser system was used for the experiments reported in this thesis. The system is composed of a Nd:glass laser, a vacuum chamber, a system for plasma detection and the necessary ancillary equipment to support each subsystem. In this thesis the floating double electrostatic probe detector was used for plasma diagnostics. A complete explanation of the floating double probe used is contained in Appendix E.

#### A. THE LASER SYSTEM DESCRIPTION

A block diagram of the system components used in this thesis is pictured in Figure 17. The Nd:glass laser subsystem is centered around the KORAD K-1500 Q-switched neodymium in glass laser [57]. The laser output energy is controlled by varying the voltage applied to the oscillator (K-1) and the amplifier (K-2). The energy range of the laser beam is 2.5 to 15 J. and the power of the beam is approximately 340 MW. The pulse half width value is 25 nsec. The laser pulse shape is pictured in Figure 18.



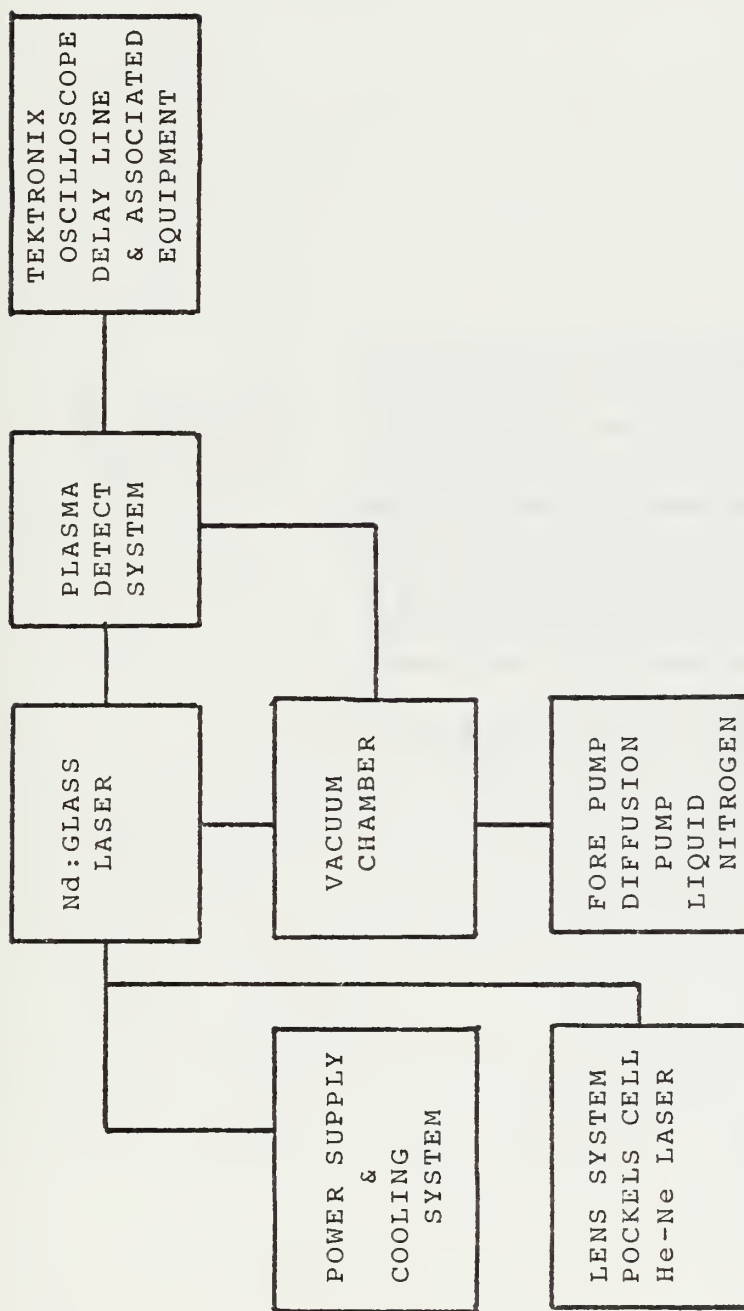


FIGURE 17. BLOCK DIAGRAM OF THE LASER SYSTEM COMPONENTS



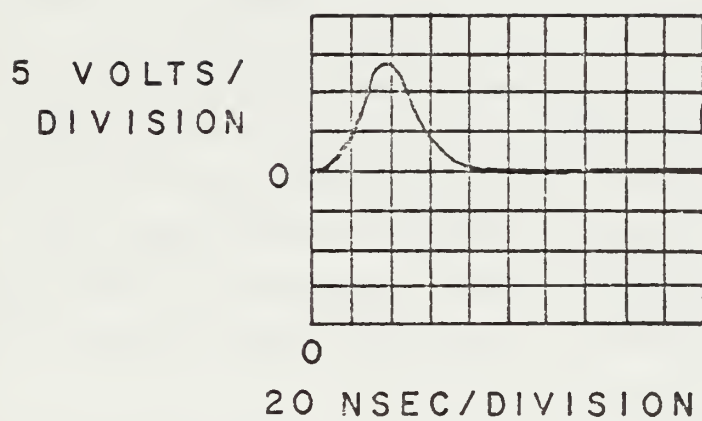


FIGURE 18. THE LASER PULSE SHAPE



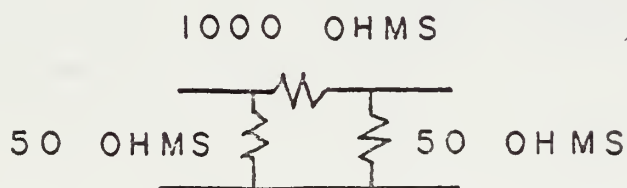
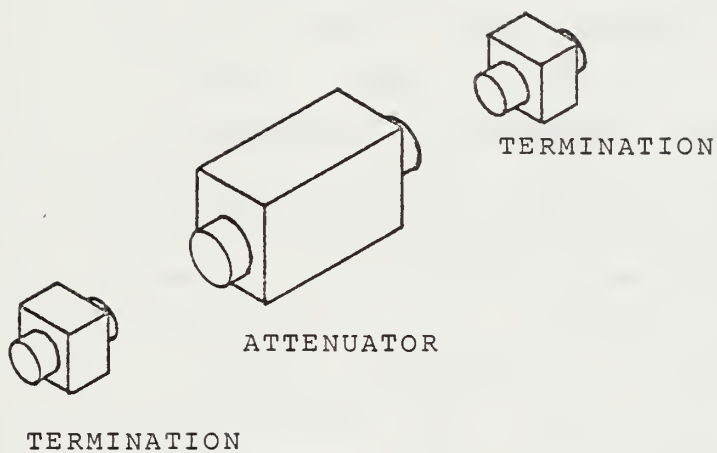


A 30 cm focal length lens was used to focus the laser beam down to a 0.01 cm diameter, circular spot size. The flux density delivered under these conditions is about  $4.4 \times 10^{10} \text{ W/cm}^2$ . A general description of the KORAD Nd:glass laser physics is given by Maiman [34]. The system installed at Naval Postgraduate School Laser-Plasma Laboratory is detailed by Davis [16].

Each laser pulse passes through the beam splitter which provides signals for two functions. The first purpose the beam splitter serves is to reflect an electromagnetic signal to the magnesium oxide photodiode detector (K-D1). That signal is fed to a Tektronix 564B storage oscilloscope which integrates it to measure the laser pulse energy. The other function of the beam splitter is to provide a trigger signal for the Tektronix 7904 oscilloscope via a photodiode detector. That insures reproducible triggering of the 7904 oscilloscope at the same instant of time. It also marks the arrival of the plasma probe detection signal on every shot without losing part of the laser pulse signal. Both the probe signal and the laser pulse can be displayed on every laser shot.

The laser pulse signal received by the MgO photodiode detector from the beam splitter was much greater (about 10 times) than the plasma signal from the probe. To scale it down to a signal that can be displayed with the probe signal in the same trace, a Tektronix Model 3752 attenuator box was used with a 50 ohm resistor at either end and connected on one side to the Tektronix 7704 oscilloscope and the other side to the coaxial cable from the MgO photodiode detector. It acted as a voltage divider for the terminated signal, reducing its value (see Figure 19.) There are 10 attenuators of various resistances for ready use.





ELECTRIC CIRCUIT

FIGURE 19. THE SIGNAL ATTENUATOR



If none fits the experiment requirements, it is a simple matter to change the resistance in the attenuator by removing the screws in the cover and soldering in a different resistance.

When the laser beam hits the target in the vacuum chamber with a flux density greater than  $10^7 \text{ W/cm}^2$ , a plasma plume is formed. This plume was the subject under investigation in this research.

The laser rod cooling system cools the rods in the K-2 amplifier and the K-1 oscillator. There is a small refrigerator, a water pump, a water filter, two thermometers, a thermostatic temperature control and a reservoir of deionized water in the cooling system.

There are four power devices associated with control of the laser beam. A 10 kilovolt power supply provides power to the K-2 amplifier. A 5 kilovolt power supply provides power to the K-1 oscillator. The shutter control is associated with the Pockels cell control of the laser pulse shape and the small 2000 volt HV-1565 power supply energizes the MgO photodiode detector.

A CW HeNe laser provides visual alignment and target positioning reference for the laser system. The laser system is diagrammed in Figure 20.



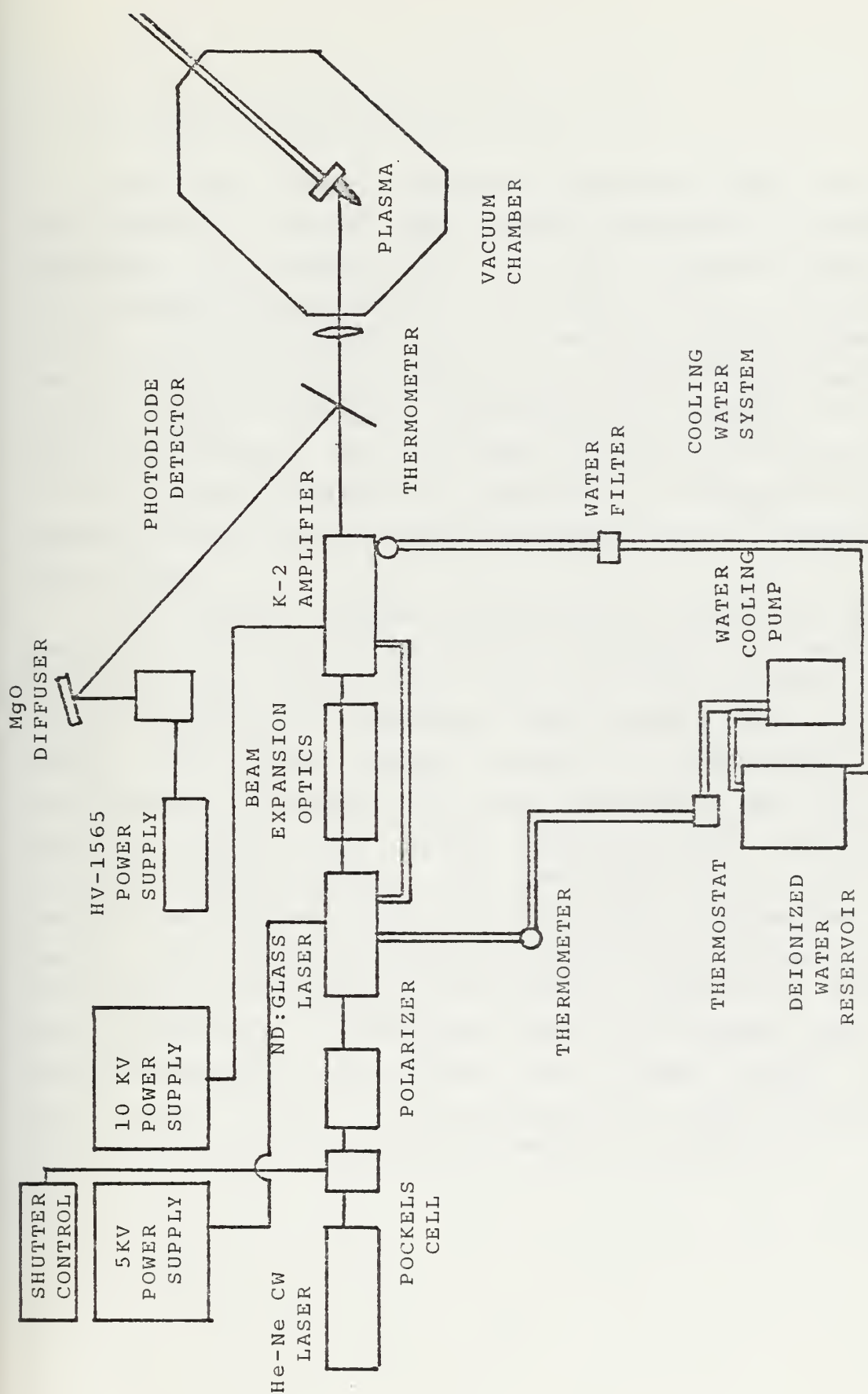


FIGURE 20. THE Nd:GLASS LASER SUBSYSTEM





## B. THE PLASMA DETECTION COMPONENTS

For the detector subsystem associated with the laser (see Figure 21) there are various diagnostic techniques available for investigating the laser produced plasma. In the experimentation relevant to this thesis, a floating double probe (see Figure 22) was used for plasma detection. The laboratory is also equipped to do research with magnetic probes, single filament electrostatic probes and X-ray detection devices. The two sizes of plates for the top port in the vacuum chamber are tapped for 0.5 cm and 0.25 inch diameter probe shafts. Other detectors can be designed to the system.

The plasma detector subsystem is made up of the photodiode to detect the initial laser pulse, a photodiode to trigger the oscilloscope on which the plasma energy signal appears, a Tektronix 564B storage oscilloscope to measure the laser pulse energy, a Tektronix 7704 oscilloscope to display the laser pulse shape and the plasma detector signal, the plasma detector (an electrostatic floating double probe), the detector power supply and coaxial cable delay lines for time signal coordination. The delay line from the probe to the 7704 oscilloscope allows for signal time lag by a fixed amount to match the relative time dependence of the laser pulse, the trigger pulse, and the electrostatic probe signal. The signal speed through the coaxial cable is two-thirds the speed of light. A schematic of this subsystem is shown in Figure 21.



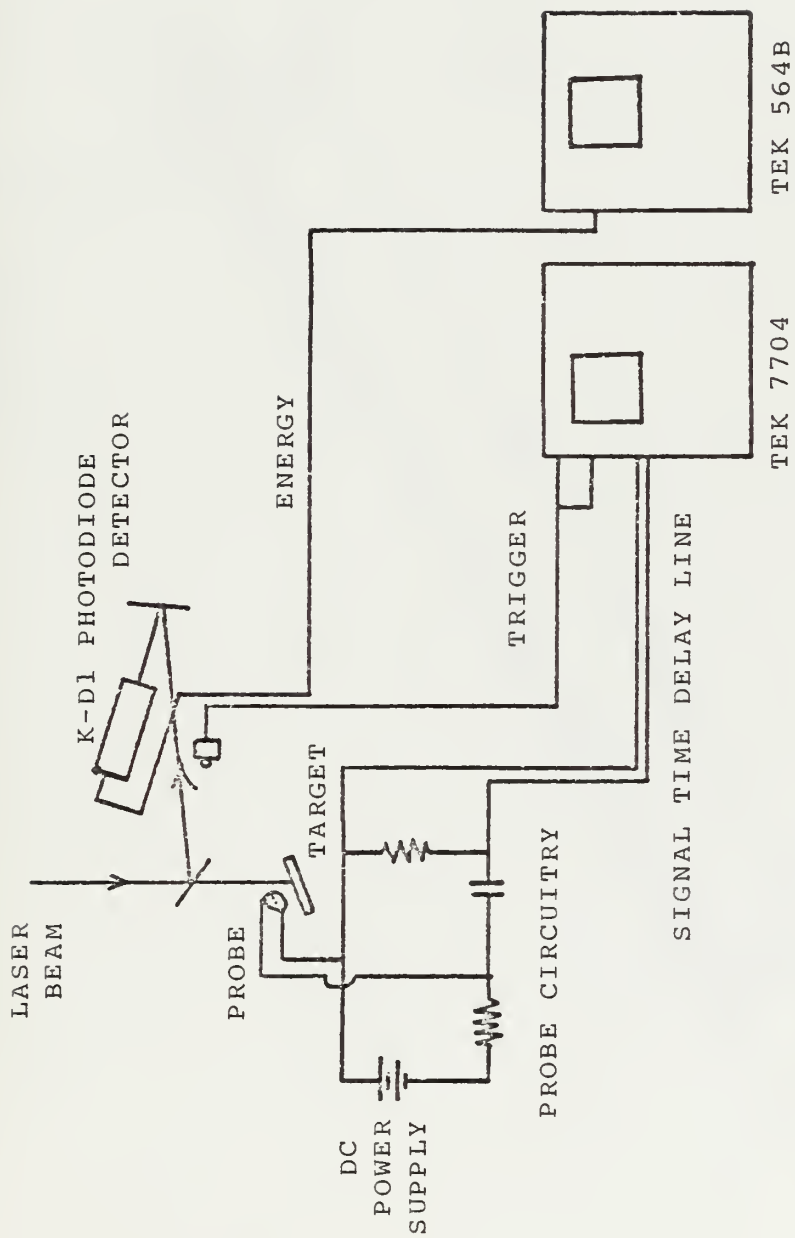


FIGURE 21. THE DETECTOR SUBSYSTEM



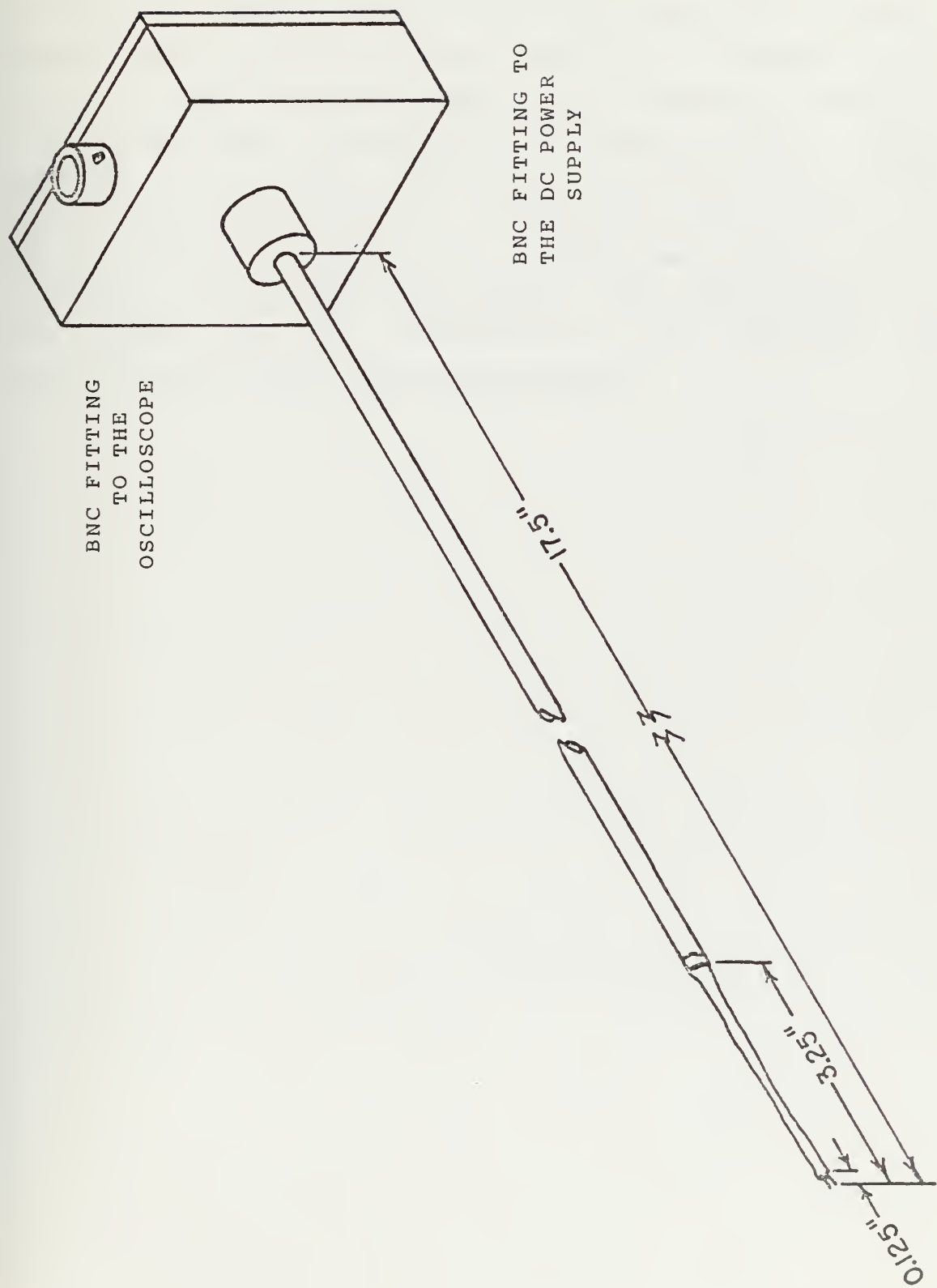


FIGURE 22. A FLOATING DOUBLE PROBE



When the laser beam is fired, the firing key also energizes the camera on the oscilloscope. A Tektronix Model 3 automatic shutter control and camera mount and a Polaroid camera (Polaroid 410 film) were used for the picture taking.

A stray triggering signal will occasionally arrive at the oscilloscope, triggering the camera early. Nothing appears on the scope trace but a straight line. If this happens too often, check the oscilloscope sensitivity and slope settings. They were a very fine, easy to disturb adjustment during these experiments. The time constant for any cable can be determined on the Tektronix 519 oscilloscope by the following procedure.





## 1. Time Length of Coaxial Cables

Plug in the scope and turn it "ON".

Connect the RATE GENERATOR +RATE 50  $\Omega$  terminal into the INPUTS SIGNAL 125  $\Omega$  terminal through a T50/N125 2W connector.

On the TRIGGER panel, set the TRIGGER SOURCE to RATE GEN. The room should be in semidarkness to read the purple oscilloscope trace.

Set the RATE GENERATOR panel MULTIPLIER switch to X100 and the CYCLES/SEC X MULT. switch between 6 and 12.

On the TRIGGER panel, set the GAIN to NORMAL, the FUNCTION switch to PULSE and the PULSE AMPLITUDE OR SYNC switch to the black arrow indication.

Set the TIME BASE panel NANOSEC/CM switch to 10 and the DELAY knob to the approximate center of scale.

Insert a coaxial cable connector tee at the INPUTS SIGNAL 125  $\Omega$  line on the end of the T50/N125 adapter.

Reconnect the +RATE 50  $\Omega$  lead to one side of the tee and the cable to be measured to the other side of the tee.

Look on the scope trace. The time from the leading edge to the signal is the time it takes for a signal to go up and back on the cable so divide it by two and that is the cable's time delay.



### C. THE VACUUM CHAMBER

The vacuum chamber subsystem is the final part of the laser system (see Figure 23). It consists of the vacuum chamber, a gas bleeder system, the target and target holder, an oil diffusion pump, a liquid nitrogen cold trap, a mechanical fore pump, a vacuum chamber thermocouple gauge, an ion gauge in the diffusion pump, a thermocouple gauge in the fore pump vacuum line, an ion gauge in the vacuum chamber and a meter to read the pressure at each gauge (GMA-201, RG-A, and IONIZATION GAUGE CONTROLLER). The forepump brings the system vacuum pressure down to about  $10^{-13}$  torr. At  $10^{-3}$  torr the oil diffusion pump takes over and can reduce the pressure in the vacuum chamber further to about  $10^{-7}$  torr. The liquid nitrogen trap above the diffusion pump acts as a condenser for the hot oil droplets coming up from the heater. The diffusion pump exterior is cooled by an open ended tap water cooling system that drains off into a well outside of the building.

The vacuum chamber can be isolated from the vacuum pumps by the chamber gate valve. The vacuum chamber has five large side ports for instrumentation and observation, two small side ports, and another large port on top, also for diagnostic instrumentation. The target (usually a metal disc) is suspended in the vacuum chamber at the end of the threaded metal rod with a knurled handle outside of the chamber. The rod passes through the vacuum chamber wall in a vacuum fitting to facilitate the experiment operation by exposing a clean target surface to the laser beam periodically without breaking the chamber vacuum.



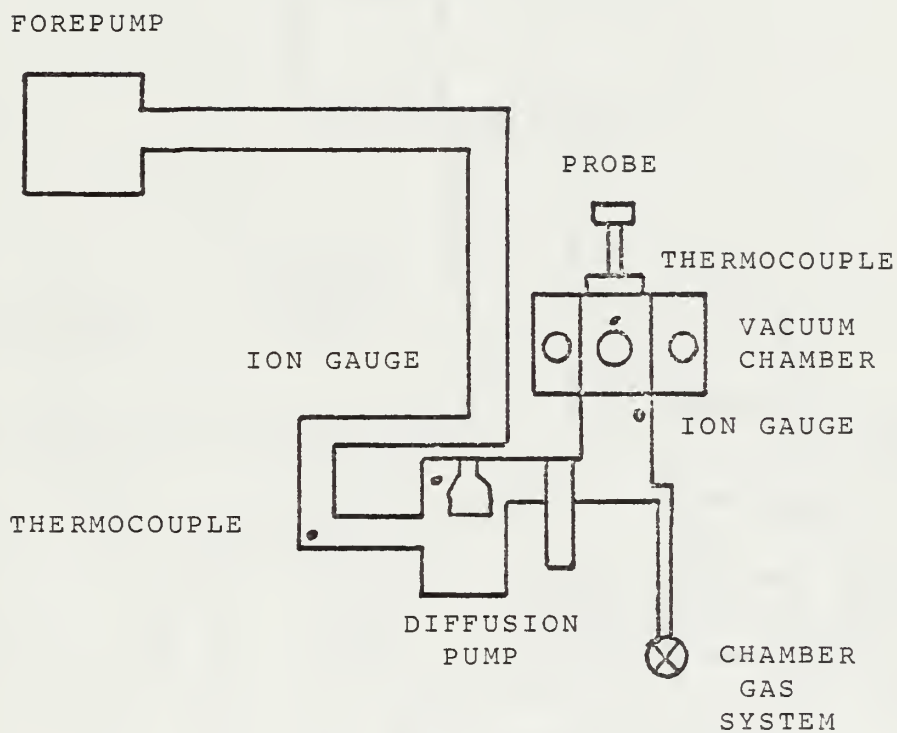


FIGURE 23. THE VACUUM CHAMBER SUBSYSTEM



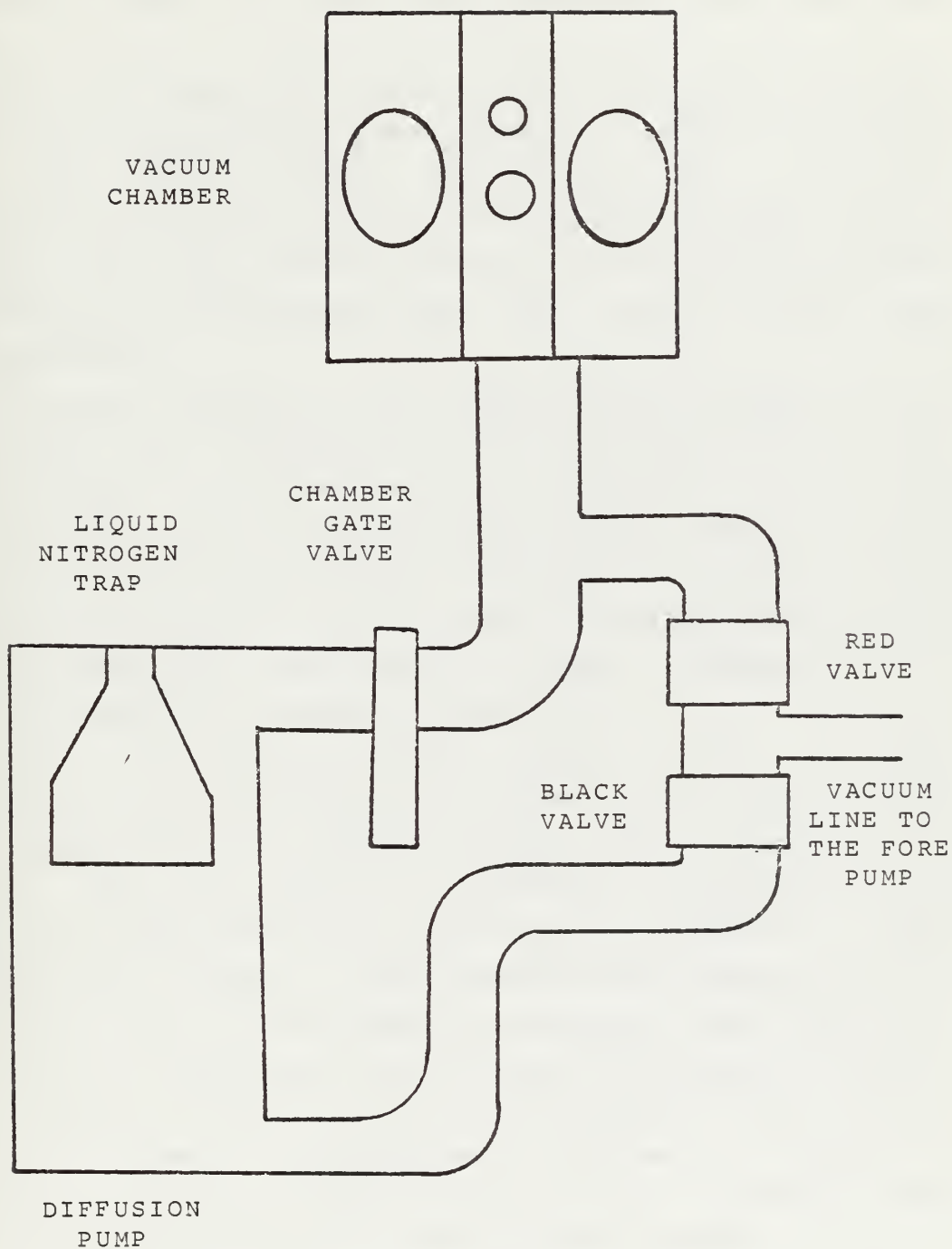


FIGURE 24. ROUGHING VALVE OPERATION





The various gauges (two thermocouple and two ion gauges) monitor the system pressure at various points in the system (see Figure 23). Each gauge is attached to an electronic meter to read the pressures at the monitoring points.

The forepump was used to rough pump both the vacuum chamber and the diffusion pump through a system of valves under the vacuum chamber (see Figure 24). Once the diffusion pump has been cut in to the vacuum chamber the red roughing valve must remain closed to prevent back pressure. The procedures in the Laser Light Off section cover this idea thoroughly.

A recent addition to the vacuum chamber subsystem for fire safety and protection of the diffusion pump are two relay switches. A thermal switch was added to prevent the oil diffusion pump from over heating and burning out the heater coil, and a flow switch was added to shut the oil diffusion pump off if the flow of the cooling water to the pump is interrupted. The electric circuit schematic for the switching devices is shown in Figure 25.

The laser system safety aspects must be well understood by the researcher. To remember the standard Navy safety precautions for working around high voltages is a definite way to avoid an accident. Familiarity and overlocking common sense for the sake of expediency is just as dangerous around a high powered laser system as it is aboard ship. All of the safety interlocks in the world will not protect a technician from improperly grounded or shorted system safety features. A very good summary of the safety aspects of lasers is contained in Chapter 7 of Ready [42] and should be read by all laser system operators often enough for their lessons to become second nature.

The laser system operating procedures are included in the following sections to give future students ready access to lessons already learned about the equipment operation.



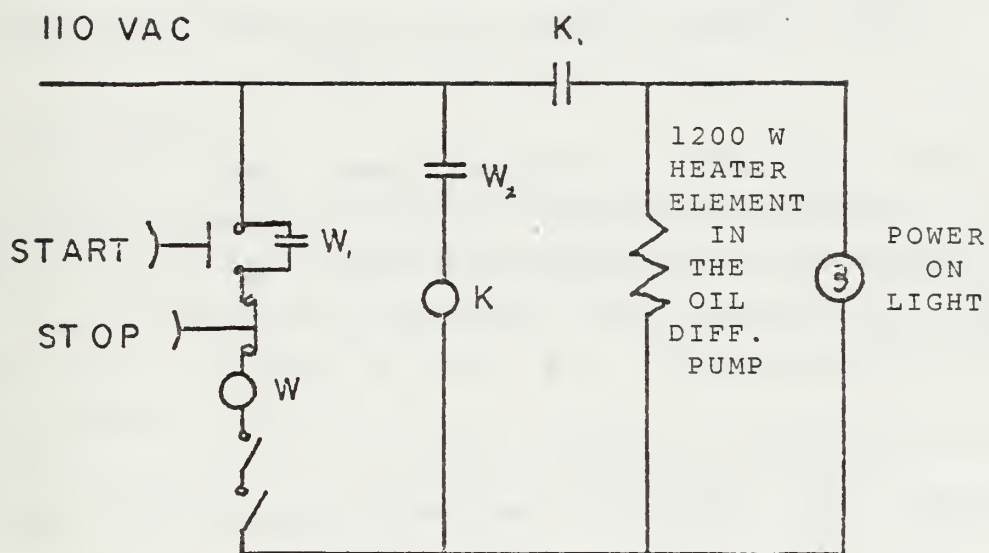


FIGURE 25. DUAL RELAY INTERLOCKS (W,K) FOR DIFFUSION PUMP OPERATOR



## D. LASER OPERATING PROCEDURES

### 1. Nd:Glass Laser Light-Off Procedures

#### 1. Forepump

Close star shaped vacuum vent.

Push forepump "START" button.

Start the air conditioners to dehumidify the room by switching #11c and #9b in the circuit breaker panel.

#### 2. Ion Gauges

Turn on the power switch to GMA-201. This is a thermocouple gauge to measure the chamber pressure. Select station #1 and this meter will operate in an automatic mode.

Turn on the power to RG-3A. The thermocouple gauge on this meter is set at T.C. #1. It measures the forepump rough vacuum.

The degas switch sends a current through the ion tube to expel adsorbed gas from the electrodes. The system has to be at  $10^{-5}$  torr or less to use this feature.

The current set, current adjust, and read current indicators let you observe the ion gauge grid parameters from time to time.

#### 3. Diffusion Pump

Turn on the cooling water.

Don't turn on the diffusion pump until the forepump has been operating for about twenty minutes and the pressure in the diffusion pump system is less than one hundred microns because the diffusion pump will not pump down in greater pressures. Also operating at excessive pressure destroys the



pump. The diffusion coil overheats and evaporates and the heating coil burns out.

Make sure the chamber gate valve is closed.

The black valve under the chamber should be open.

The red valve under the chamber should be shut.

Push the diffusion pump "START" button. The red "ON" light on the metal relay box below the button will come on. The relay box is wired to a temperature sensitive thermal switch on the diffusion pump and a pressure switch on the cooling water line. The thermal switch will shut off the diffusion pump if it overheats and the pressure switch will shut off the diffusion pump if the cooling water line loses back pressure, i.e. if the cooling water is shut off before the pump or the cooling line starts to leak.

#### 4. Ion Gauges

When the diffusion pump has been on for ten minutes, the pressure in the diffusion pump system will be sufficiently low to turn on the ion gauge in the diffusion pump system without burning out the filament. A vacuum of about  $10^{-3}$  torr or less is required or an automatic meter feature will shut it off.

Set the pressure multiplier selector to  $10^{-4}$ .

Adjust the zero on the ionization gauge meter.

Push the filament "ON" button. The red light should come on and the ion gauge tube filament at the diffusion pump should start to glow.

#### 5. Diffusion Pump Control

Let the diffusion pump operate for about twenty minutes. While recording the ion gauge pressure and the forepump thermocouple pressure, note that whenever you light off the electron tube ion gauge detectors, the wires and glass in the system tend to heat up. There is a temporary





rise in pressure due to the degassing at the solid surfaces in the system which implies increased pressure.

When the pressure in the diffusion pump chamber has reached  $10^{-5}$  torr (in about twenty minutes), add the liquid nitrogen to the cold trap. The pressure will drop two more orders of magnitude to about  $4 \times 10^{-7}$  torr. This step is optional if  $10^{-5}$  is an acceptable chamber pressure.

#### 6. Opening the Chamber to Vacuum

Turn the ion gauge scale to  $10^{-4}$ , because when the gate valve is opened there will be a rush of pressure to the diffusion pump which will cause the detector to impulse to about  $5 \times 10^{-4}$  torr.

Make sure the chamber vacuum is tight.

Close the black valve below the chamber.

Crack the red valve when satisfied that there are no leaks.

If the pressure, as indicated by the thermocouple gauge, is decreasing, then the chamber is probably vacuum tight. If a very porous or very effusive material (tape, paper, fresh paint, etc.) is put in the chamber, it may take a very long time to get a reading below one or two hundred microns.

When the pressure in the chamber reaches seventy-five microns or less, close the red valve.

Open the black valve.

Crack the chamber gate valve open.

Check to see that the pressure in the chamber is remaining at one hundred microns or less and gradually open the gate valve. If the pressure does not decrease, close the gate valve and return to the beginning of this procedure.

Continue to record the ion gauge pressure, forepump



pressure, and chamber pressure for about ten minutes to insure the system is vacuum tight.

## 7. Chamber Ion Gauge

This detector is easily burnt out and hard to replace so it is imperative that the system pump for about fifteen minutes before turning it on and that it be allowed to cool off for fifteen minutes before the chamber is returned to atmospheric pressure. Diffusion pump pressure should be of the order of  $5 \times 10^{-6}$  torr or less when the chamber ion gauge is turned on.

Set the ionization gauge controller power switch to "CN".

Wait about thirty seconds for it to warm up.

Select pressure 11 on the function switch.

Push meter zero-to-check and adjust as required.

Select emission current 3.2-10 mA.

Now select "AUTO" on the power switch. This automatically lets the meter circuit select the vacuum scale.

Push the filament "ON" button.

The initial reading of the gauge meter will be in the range of  $2 \times 10^{-5}$  torr due to out-gassing.

The final pressure should be reached in five minutes at about  $5 \times 10^{-6}$  torr. The limit of this vacuum system is a chamber pressure of  $1.5 \times 10^{-6}$  torr and diffusion pump pressure at about  $9 \times 10^{-8}$  torr.

The chamber is now in vacuum and ready for the laser experiments. Note that the laser shots create plasmas which increase the pressure readings in the system briefly. The chamber ion gauge can automatically compensate for the change by shifting scales but the diffusion pump ion gauge does not have this feature so it is good procedure to set it



-4  
to the 10 scale when shooting a target in the chamber.

#### 8. The Laser

First turn on the continuous He-Ne laser to see where the Nd laser beam will be going. Turn the switch at the back of the He-Ne laser to "ON". Wait three seconds then push the switch to "START". Be careful not to move the laser by rough handling when switching because it is optically alligned.

#### 9. The Laser Cooling System

Turn on the right switch at the water pump. The cooling water is special deionized water. Do not use tap water in this system. Check to see that the water bubbles through the transparent tee over the reservoir. If it doesn't, there are problems in the cooling water system.

Turn on the left switch to start the refrigerator. There is an automatic temperature control just under the transparent tee that can be adjusted with a screwdriver to control the cooling water temperature.

#### 10. Laser Power Supplies

Push the shutter control power button. It will light up when power comes on.

Switch on the five kilovolt power supply. The "DUMP" light will come on when power is on.

Switch on the ten kilovolt power supply. The "DUMP" light will come on when power is on. Let power supplies warm up for five minutes before using them.

Switch "AC ON" switch to the HV-1565 power supply.

Switch "HV ON" switch to the HV-1565 power supply.

Wait for ten minutes then check the temperature over the 10KV power supply. Safe limits for power supply operation are 25° to 35° C.

Check and record the laser cooling water temperatures





at the K-2 amplifier. Safe laser cooling water temperature is about 20° C. Monitor the temperatures occasionally. If the cooling water is inadvertently overlooked and not turned on, the temperature will go up on each shot. If that happens DO NOT TURN ON THE COOLING WATER, shut the whole system off for at least two hours so the rod in the laser will cool off naturally. If the cooling water is turned on the sudden heat flow will break the glass rod, ruining the laser (this has happened).

#### 11. Experimental Equipment

Turn on all oscilloscopes, cameras, experiment equipment power supplies, and all other equipment for the experiment to be run.

#### 12. Laser Firing

Blow off all optical surfaces of the laser with an air bulb before starting. Dust and dirt will tend to cause pitting on the optical surfaces whenever the laser is fired. Do not blow on any optical surface with your breath. Moisture will deposit and, like dust, will tend to pit the surface.

There are two methods of firing the Nd laser, local and remote. The local method is from the 10KV power supply and the remote is from a specially constructed control box.

When ready to charge the power supplies to shoot the laser, announce the fact to all in the room as a safety precaution.

Put your safety glasses in place. Do not proceed until every one has on safety glasses.

When everyone is ready, push the "CHARGE" button. The voltage will start coming up on the meters at the power supplies. Chiming bells will toll at the rate of about two per second until the system is completely charged. When the power supplies are ready to fire the laser, a continuous monotone whistle will sound. The ready light will come on





on the remote control and the "FIRE" light will come on at the 10KV and 5KV power supplies.

If for some reason the shot is to be aborted, push the "DUMP" button on the 10KV power supply or the remote control box. Do not "DUMP" or "FIRE" before the power supplies are fully charged because it causes excessive currents in power supply control relays and tends to burn them out.

To shoot the laser, push the "FIRE" button on the 10KV power supply or on the remote control box.

The time between consecutive shots should be sixty seconds or more to allow time for the glass rod in the laser to recover a constant temperature gradient.

Check the temperature over the 10KV power supply air vent occasionally to detect any overheating.

## 2. Shut Down Procedures

### 1. Experiment Equipment

Shut off all oscilloscopes, cameras, experiment power supplies, and other experiment equipment power.

### 2. The Laser

Turn off the 10KV power supply.

Turn off the 5KV power supply.

Turn off the shutter control power by pushing the power button. The light turns off when power goes out.

Turn off the HV-1565 high voltage.

Turn off the HV-1565 AC.

Turn off the continuous He-Ne laser.

Let laser cooling water flow for ten minutes after the last laser shot, then turn off the two laser cooling water control switches.



### 3. Vacuum Chamber

Leave GMA-201 on indefinitely. It will not damage the meter.

Turn off the chamber ion gauge filament.

Turn off the chamber ion gauge filament power.

Close the chamber gate valve.

Let the ion gauge filament cool down for about fifteen minutes before venting the chamber. Failure to let it cool tends to burn out the ion gauge filament when the chamber is vented. The vent is located above the red valve under the chamber. Vent the chamber if desired.

### 4. Diffusion Pump

Select 10<sup>-4</sup> on the pressure multiplier switch to FC-3A.

Turn off filament to the diffusion pump ion gauge. Power can be left on continually to RG-3A without damaging the meter.

Push "STCF" button on the diffusion pump.

Let the diffusion pump cooling water continue to flow for about twenty minutes. This is an open end cooling system that dumps out in the well outside of the building inside of the theta-pinch power plant fence. The diffusion pump and the cooling water can be left on indefinitely if desired while research is in progress.

### 5. Wrap up

Turn off the air conditioners at circuit breaker switches #11c and #9b.

Leave the forepump on continuously. To shut it off when desired, push the "STOP" button and open the star shaped vent valve.



## APPENDIX B

### THE ELECTROSTATIC PROBE

The electrostatic floating double probe signal was used to determine the time at which the laser produced plasma pulse arrived at the probe location. When a DC voltage is applied between two electrodes in a neutral plasma, the ions are attracted by the negative electrode and the electrons by the positive one. The charge migration and isolation creates space charge electric fields, changing the character of the plasma neutrality. A fundamental characteristic of the behavior of a plasma is its ability to shield itself from the electric fields in and around it by Debye shielding. The sheath thus formed absorbs the potential difference exponentially within a few Debye lengths,  $\lambda_D$ , where,

$$\lambda_D = 69(T_e/n_e)^{1/2} \text{ [meters].}$$

$$T_e = [\text{°K}],$$

$$n_e = [\text{m}^{-3}].$$

Assuming  $n_i$  and  $n_e$  are approximately equal, Table 7 indicates that  $n_e$  varies from about  $1.08 \times 10^{11}$  to  $7.34 \times 10^{13}$   $[\text{cm}^{-3}]$ .  $T_e$ , calculated for this experiment by electrostatic



probe theory, was about 50 eV. On the same experimental apparatus, Shewchuk [49], using X-ray diagnostics, got an electron temperature at the target surface of 162 eV. Williamson [61] also used a temperature of 162 eV in his experiments using magnetic probes at the target surface. Bricks [10] in earlier research used an average temperature of 100 eV for his calculations. A plasma temperature of 50 eV is consistent with Shewchuk's value two cm from the target surface.

To use the electrostatic probe theory in discussions of the plasma characteristics, the probe radius must be much greater than the Debye length which is the case for a Debye length of about  $10^{-3}$  cm at two cm from the target surface. Using  $n_e = 7.34 \times 10^{14} \text{ cm}^{-3}$  and  $T_e = 50 \text{ eV}$ , the minimum Debye length at two cm from the target was  $1.94 \times 10^{-4}$  cm. Using  $n_e = 1.1 \times 10^{11} \text{ cm}^{-3}$  and  $T_e = 162 \text{ eV}$ , the maximum value for the Debye length in the plasma right at the target surface was  $2.85 \times 10^{-2}$  cm. Then the Debye length is of the order of;

$$2.85 \times 10^{-2} > \lambda_D \geq 1.94 \times 10^{-4} \text{ cm.}$$

The probe radius was  $2.54 \times 10^{-2}$  cm which was approximately equal to the greatest possible value of the Debye length, i.e. at the target surface. The probe radius was approximately 130 times larger than the minimum Debye length measured at two centimeters from the target surface.

An advantage of the double probe system over the other types of probes is that the maximum current drawn is always





limited by the ion densities because the current is limited with the ion saturation current. In the double probe theory developed for a static plasma the saturation ion current,  $I_+$  [amp], is related to the density by the relationship

$$n_i = 1.67 I_+ (m_i / kT_e)^{1/2} / e A_p$$

where:  $A_p$  = surface area of the probe [ $\text{cm}^2$ ]  
 $n_i$  = ion concentration [ $\text{cm}^{-3}$ ]  
 $m_i$  = ion mass [gm]  
 $e$  = particle charge [ccul]  
 $kT_e$  = electron temperature [erg]  
 and 1.67 is a unitless constant.

The electron temperature can be deduced from the slope of the  $I$  versus  $V$  probe characteristic curve at  $V = 0$  (see Figure 5), using the relationship:

$$T_e = (e I_+ / 2k) (dI/dV)^{-1} [^\circ\text{K}]$$

where  $I_+$  is the saturation ion current in amps.

For the case of a streaming plasma the ion current is given [10] by:

$$I_+ = n_i Z e A_p V_{LP}$$

where:  $n_i Z e$  = average ion charge per unit volume  
 $V_{LP}$  = plasma stream velocity [cm/sec].

Or more accurately:

$$I_+ = n_i Z e (1 + s) A_p V_{LP}$$

where the coefficient,  $s$ , is included to correct for the secondary electron emission from the probe. The values of  $s$  range from 0.0 to 0.5. For tungsten probe filaments  $s$  is



approximately equal to 0.5.

For the experiment performed, the average ion densities in the plasma plume, when the probe was placed 2 cm from the target, were calculated and arranged in Table 9.

$$I_+ = V/R = n_i Z e (1 + s) A_p V_{LP}$$

where:

V = probe response voltage [volts]

A<sub>p</sub> = 2πrh, the exposed probe surface area

h = 0.32 cm, the whisker length

r = 2.54X10<sup>-2</sup> cm, the whisker radius

R = total circuit resistance in ohms

n<sub>i</sub> = average ion density at 2 cm

solving for n<sub>i</sub> using,

$$A_p = 5.1 \times 10^{-2} \text{ cm}^2$$

$$R = 1 \text{ ohm}$$

$$s = 0.5$$

$$Ze = 1.5 (1.6 \times 10^{-19}) \text{ coul}$$

then

$$n_i = 5.45 \times 10^{19} V/V_{LP} [\text{cm}^{-3}].$$



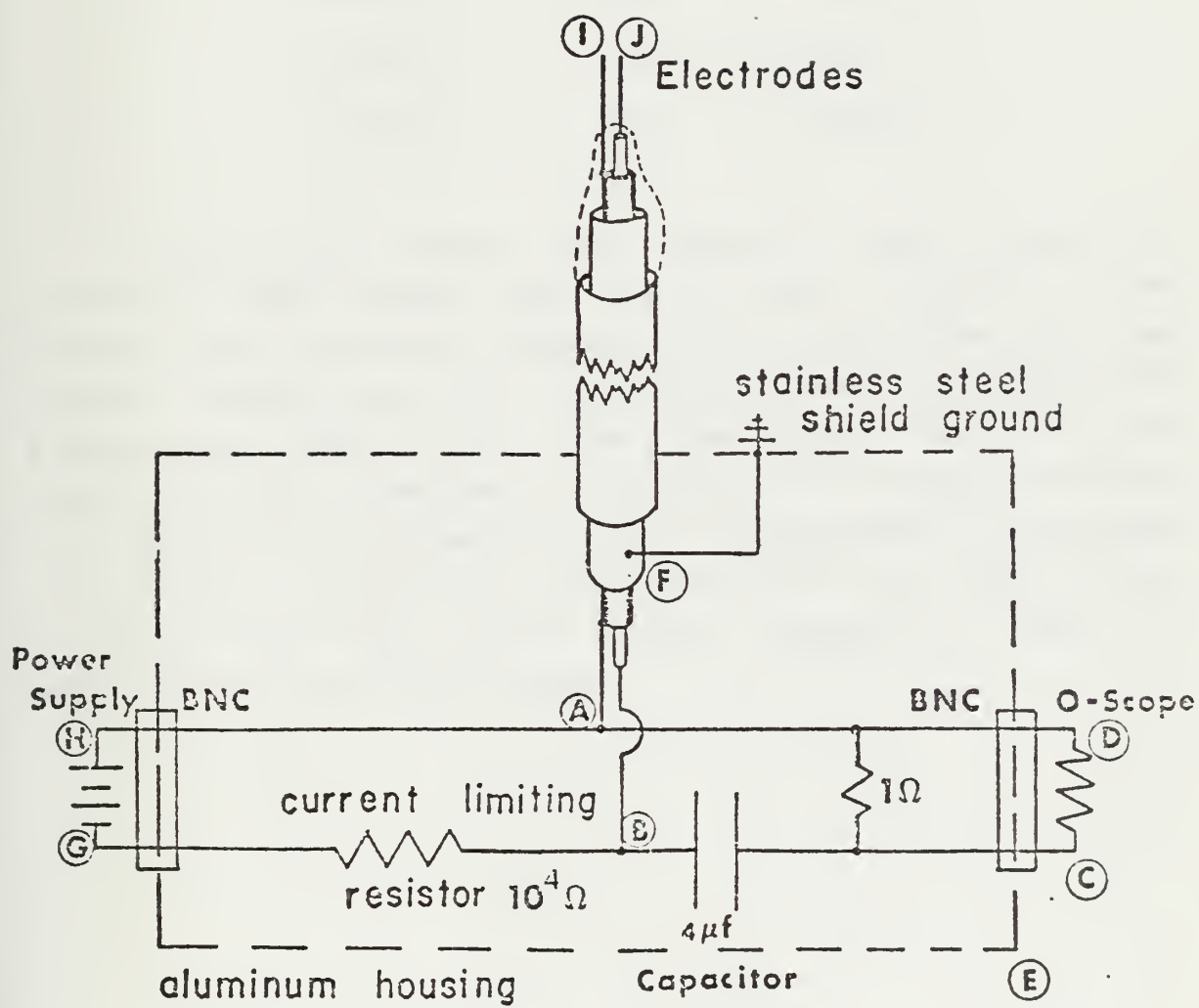


FIGURE 26. DOUBLE ELECTROSTATIC PROBE CIRCUIT DIAGRAM



Table 9. Average Ion Densities ( $n_i$ )

$V_{IF}$ [cm/sec]	$V$ [volts]	$n_i$ [cm <sup>-3</sup> ]
$4.00 \times 10^6$	3.0	$4.09 \times 10^{13}$
$5.57 \times 10^6$	7.5	$7.34 \times 10^{13}$
$1.52 \times 10^7$	2.8	$1.00 \times 10^{13}$
$3.71 \times 10^7$	0.7	$1.03 \times 10^{12}$
$1.01 \times 10^8$	0.2	$1.08 \times 10^{11}$

Electrostatic probes are actually quite simple to construct (see Figure 22). All that is needed are two suitable wire whiskers, some method to insert them into the vacuum chamber, and an electronic circuit to display the signal on an oscilloscope. The probe circuit used in this experimentation, designed by Brooks [10] is shown in Figure 26. Additional electrostatic probe construction techniques are covered in Chen [25] pages 194 thru 199. Table 10 can be used to check the probe circuit integrity. Refer to Figure 26 for the test points.





Table 10. Electrostatic Probe Circuit Verification Table

Connection	Resistance Reading Good (ohms)	Actual Probe Resistance Readings (ohms)
A to I	0	0
F to J	0	0
H to E	>100K	1M
C to F	>100K	2M
F to E	0	0
G to B	>5K	10K
L to C	1	1
H to D	0	0
E to C	1	1

Problems areas to watch for when the probe appears to be faulty are:

(1) The BNC connectors at HG and DC are not very well insulated from the probe chassis. If they ground out, they should be replaced with BNC connectors that have an insulating plastic ferrule fixed to the connector to insulate it from the chassis.

(2) The 4 microfarad capacitor went out during this experiment. It is not a standard size so extras were stocked in the laboratory in case another fails.

(3) The probe whiskers AI and EJ can break off very easily and great care must be exercised when handling the probe. Only insert and remove the probe from the vacuum chamber when necessary. Handle it as little as possible and the probability of breakage will be minimized.

(4) After forty or fifty laser shots the probe whiskers get covered with molten aluminum globules. They should be carefully cleaned off with a knife blade



at convenient intervals during the experimentation.

A 0.25 inch diameter metal tube slipped over the outside of Brooks [10] probe will provide added strength. The over all length of the probe, from the whiskers up to the chassis, should not exceed 20 cm in length. The shorter the shaft the easier it is to handle it without breaking. Very long probes have a tendency to break easily when inserting and extracting them from the vacuum chamber probe holder and are hard to store and work around. Extra shaft support for existing probes with glass shafts can be had by using chemistry laboratory stands, clamps and solid metal structural tubes.



## APPENDIX C

### THE COMPUTATIONAL ANALYSIS OF DATA

To facilitate experimental data reduction the W. R. Church Computer Center IBM 360 computer system was employed. The following references were used to write the computer programs: Gottfried [22] and Shampine [48]. The oscilloscope photograph data from each laser shot was analyzed and transferred to data cards (see Figure 27). The data taken from each oscilloscope probe signal photograph consisted of the following list of variables.

(1) The picture number, called matrix DESIG, given in a double precision form is XXXX.YYZZAA, where XXXX is the local time of the picture, YY is the day of the month that the picture was taken, ZZ is the month, and AA is the last two digits of the year.

(2) The laser shot number (the number one being a fresh target surface) was called matrix SHOT for data input and later in the program SHC for additional sorting capability.

(3) The distance of the detector probe from the target surface was called matrix D for input and DIS for sorting.

(4) The probe DC voltage bias was called BIAS.

(5) The time of the peaks in the oscilloscope pictures was called matrices T1, T2, and T3 for data input because some photographs had as many as three readable peak values. Time was changed to matrix T for



scoring and computing operations.

(6) The matrices PK1, PK2, and PK3 were used to input the peak values of the electrostatic probe signals. The matrix PK was used later in the program for computing.

(7) The laser pulse energy was designated matrix E for input and changed to EN for computing.

(8) The measurement errors for time and peak probe voltage values were recorded as matrix ERT and ERVOL respectively. These were to allow the experimental error bars to be computed and plotted.

The typical data card was punched as pictured in Figure 27. A total of 376 pictures were included in the data deck for machine analysis. Nearly as many pictures were discarded. They were unreadable because the time mark was not readable or because no peaks appeared on the oscilloscope scales picked for the shots.

The original program to execute data reduction was written in four sections. The first section was to read in the data cards (see Figure 28), the second to locate all non-zero peaks and their associated time of occurrence and change them to matrices PK and T respectively (see Figure 29). The third section, also in Figure 29, operates on the graphical peaks, computing the distance the plasma had to travel from the laser crater to the probe and using this distance to compute a velocity for each data peak. The remaining section (see Figure 30) was used to graph the data points. A computer library program DRAWP was used in this section to produce the graphs included in the results of this thesis. The original program is listed here.









As more information was required from the data, more sections had to be added to the program. Section five (see Figure 31) is a sorting routine to separate the data points by shot number. Notice that the matrices that have already served their purpose can be used again to save computer cell storage space.

Further unanswered questions about the experimental data required a subroutine to average the energy of each laser shot to see if energy had any bearing on the results. Section six (see Figure 32) was inserted just following section one and AVENER was a subroutine designed and called to average the data point energies. AVENER was listed as a subroutine. AVENER takes matrix A with an initial value  $A(1) = S1$ , averages the values  $A(1)$  to  $A(NB)$  and returns the standard deviation, SIG, and the average value of matrix A, ME to the program.



```

REAL*8 DESIG(500)/500*0./
REAL*4 NE
INTEGER*4 ITB(12)/12*0./
REAL*4 RTB(28)/28*0./
REAL*4 CVEL(600)/600*0./, SHQ(600)/600*0./, EN(600)/600*0./, T(600)/60
REAL*4 DIS(600)/600*0./, DPK(600)/600*0./
10*0./, PK(600)/600*0./, VEL(600)/600*0./, T1(400)/400*0./, T2(400)
REAL*4 SHCT(400)/400*0./, BIAS(400)/400*0./, PK2(400)/400*0./, PK3(400
1)/400*0./, T3(400)/400*0./, PK1(400)/400*0./, EFT(400)/400*0./, ERVCL(400
2)/400*0./, E(400)/400*0./, D(400)/400*0./
3)/400*0./
NC=1
CC 11 N1=1, 500
1C REAC(5,100)DESIG(N1), SHCT(N1), D(N1), BIAS(N1), T1(N1), FKL(N1), T2(N1)
100 1, PK2(N1), T3(N1), PK3(N1), E(N1), ERT(N1), ERVCL(N1)
100 1), F(5,3)
11 F(DESIG(N1).EQ.0.0) GC TO 13
11 CC CONTINUE
11 CC CONTINUE

```

# SECTION 1. DATA INPUT

FIGURE 28. COMPUTER PROGRAM SECTION ONE



```

      I=1
      N=0
30  CCNTINUE
      N=N+1
      IF(CESIG(N).LE..01) GC TO 30
      IF(T1(N).LE..01) GC TO 70
      FK(I)=FK1(N)/BIAS(N)
      T(I)=T1(N)
      N=N+1
      GC TO 21
40  CCNTINUE
      I=I+1
70  CCNTINUE
      IF(T2(N).LE..01) GC TO 80
      FK(I)=FK2(N)/BIAS(N)
      T(I)=T2(N)
      N=N+2
      GC TO 21
50  CCNTINUE
      I=I+1
80  CCNTINUE
      IF(T3(N).LE..01) GC TO 90
      FK(I)=FK3(N)/BIAS(N)
      T(I)=T3(N)
      N=N+3
      GC TO 21
60  CCNTINUE
      I=I+1
      GC TO 90

```

SECTION 2. LOCATES ALL NON-ZERO DATA POINTS

```

21  CCNTINUE
      EN(I)=E(N)
      SHC(I)=SHOT(N)
      DIS(I)=C(N)+(.01*(SHOT(N)-1.))
      IF(T(I).LE..01) GC TO 110
      VEL(I)=(DIS(I)/T(I))*1000000000.
      IF(N3.EC.3) GO TO 60
      IF(N3.EC.2) GO TO 50
      IF(N3.EC.1) GO TO 40
30  CCNTINUE

```

SECTION 3. COMPUTES PLASMA ION VELOCITIES  
FOR EACH DATA POINT

FIGURE 29. COMPUTER PROGRAM SECTION TWO AND SECTION THREE





```

ITE(2)=1
ITE(3)=8
ITE(4)=10
ITE(10)=2
ITE(12)=1
RTE(1)=.2
RTE(2)=1.E7
ECLIVALENCE (TIT1,RTB(5))
REAL*8 TIT1(12)
300 READ (5,300) TIT1
FORMAT (6A8)
CALL DRAWP (N1,T1,BIAS,ITB,RTB)
ECLIVALENCE (TIT1,RTB(5))
READ (5,300) TIT1
CALL DRAWP (N2,T2,SHOT,ITB,RTB)
ECLIVALENCE (TIT1,RTB(5))
READ (5,300) TIT1
CALL DRAWP (N3,T3,E,ITB,RTB)
ECLIVALENCE (TIT1,RTB(5))
READ (5,300) TIT1
CALL DRAWP (N4,PK1,C,ITE,RTB)
ECLIVALENCE (TIT1,RTB(5))
READ (5,300) TIT1
CALL DRAWP (N5,PK2,SHOT1,ITB,RTB)
ECLIVALENCE (TIT1,RTB(5))
READ (5,300) TIT1
110 CALL DRAWP (N6,PK3,VEL1,ITB,RTB)
CONTINUE
STOP
END

```

FIGURE 30. COMPUTER PROGRAM SECTION FOUR



```

N1=1
N2=1
N3=1
N4=1
N5=1
N6=1
N7=1
N8=1
N9=1
N10=1
N11=1
N12=1
N13=1
N14=1
N15=1
N16=1
N17=1
N18=1
N19=1
N20=1
N21=1
N22=1
N23=1
N24=1
N25=1
N26=1
N27=1
N28=1
N29=1
N30=1
N31=1
N32=1
N33=1
N34=1
N35=1
N36=1
N37=1
N38=1
N39=1
N40=1
N41=1
N42=1
N43=1
N44=1
N45=1
N46=1
N47=1
N48=1
N49=1
N50=1
N51=1
N52=1
N53=1
N54=1
N55=1
N56=1
N57=1
N58=1
N59=1
N60=1
N61=1
N62=1
N63=1
N64=1
N65=1
N66=1
N67=1
N68=1
N69=1
N70=1
N71=1
N72=1
N73=1
N74=1
N75=1
N76=1
N77=1
N78=1
N79=1
N80=1
N81=1
N82=1
N83=1
N84=1
N85=1
N86=1
N87=1
N88=1
N89=1
N90=1
N91=1
N92=1
N93=1
N94=1
N95=1
N96=1
N97=1
N98=1
N99=1
N100=1
N101=1
N102=1
N103=1
N104=1
N105=1
N106=1
N107=1
N108=1
N109=1
N110=1
N111=1
N112=1
N113=1
N114=1
N115=1
N116=1
N117=1
N118=1
N119=1
N120=1
N121=1
N122=1
N123=1
N124=1
N125=1
N126=1
N127=1
N128=1
N129=1
N130=1
N131=1
N132=1
N133=1
N134=1
N135=1
N136=1
N137=1
N138=1
N139=1
N140=1
N141=1
N142=1
N143=1
N144=1
N145=1
N146=1
N147=1
N148=1
N149=1
N150=1
N151=1
N152=1
N153=1
N154=1
N155=1
N156=1
N157=1
N158=1
N159=1
N160=1
N161=1
N162=1
N163=1
N164=1
N165=1
N166=1
N167=1
N168=1
N169=1
N170=1
N171=1
N172=1
N173=1
N174=1
N175=1
N176=1
N177=1
N178=1
N179=1
N180=1
N181=1
N182=1
N183=1
N184=1
N185=1
N186=1
N187=1
N188=1
N189=1
N190=1
N191=1
N192=1
N193=1
N194=1
N195=1
N196=1
N197=1
N198=1
N199=1
N200=1
N201=1
N202=1
N203=1
N204=1
N205=1
N206=1
N207=1
N208=1
N209=1
N210=1
N211=1
N212=1
N213=1
N214=1
N215=1
N216=1
N217=1
N218=1
N219=1
N220=1
N221=1
N222=1
N223=1
N224=1
N225=1
N226=1
N227=1
N228=1
N229=1
N230=1
N231=1
N232=1
N233=1
N234=1
N235=1
N236=1
N237=1
N238=1
N239=1
N240=1
N241=1
N242=1
N243=1
N244=1
N245=1
N246=1
N247=1
N248=1
N249=1
N250=1
N251=1
N252=1
N253=1
N254=1
N255=1
N256=1
N257=1
N258=1
N259=1
N260=1
N261=1
N262=1
N263=1
N264=1
N265=1
N266=1
N267=1
N268=1
N269=1
N270=1
N271=1
N272=1
N273=1
N274=1
N275=1
N276=1
N277=1
N278=1
N279=1
N280=1
N281=1
N282=1
N283=1
N284=1
N285=1
N286=1
N287=1
N288=1
N289=1
N290=1
N291=1
N292=1
N293=1
N294=1
N295=1
N296=1
N297=1
N298=1
N299=1
N300=1
N301=1
N302=1
N303=1
N304=1
N305=1
N306=1
N307=1
N308=1
N309=1
N310=1
N311=1
N312=1
N313=1
N314=1
N315=1
N316=1
N317=1
N318=1
N319=1
N320=1
N321=1
N322=1
N323=1
N324=1
N325=1
N326=1
N327=1
N328=1
N329=1
N330=1
N331=1
N332=1
N333=1
N334=1
N335=1
N336=1
N337=1
N338=1
N339=1
N340=1
N341=1
N342=1
N343=1
N344=1
N345=1
N346=1
N347=1
N348=1
N349=1
N350=1
N351=1
N352=1
N353=1
N354=1
N355=1
N356=1
N357=1
N358=1
N359=1
N360=1
N361=1
N362=1
N363=1
N364=1
N365=1
N366=1
N367=1
N368=1
N369=1
N370=1
N371=1
N372=1
N373=1
N374=1
N375=1
N376=1
N377=1
N378=1
N379=1
N380=1
N381=1
N382=1
N383=1
N384=1
N385=1
N386=1
N387=1
N388=1
N389=1
N390=1
N391=1
N392=1
N393=1
N394=1
N395=1
N396=1
N397=1
N398=1
N399=1
N400=1
N401=1
N402=1
N403=1
N404=1
N405=1
N406=1
N407=1
N408=1
N409=1
N410=1
N411=1
N412=1
N413=1
N414=1
N415=1
N416=1
N417=1
N418=1
N419=1
N420=1
N421=1
N422=1
N423=1
N424=1
N425=1
N426=1
N427=1
N428=1
N429=1
N430=1
N431=1
N432=1
N433=1
N434=1
N435=1
N436=1
N437=1
N438=1
N439=1
N440=1
N441=1
N442=1
N443=1
N444=1
N445=1
N446=1
N447=1
N448=1
N449=1
N450=1
N451=1
N452=1
N453=1
N454=1
N455=1
N456=1
N457=1
N458=1
N459=1
N460=1
N461=1
N462=1
N463=1
N464=1
N465=1
N466=1
N467=1
N468=1
N469=1
N470=1
N471=1
N472=1
N473=1
N474=1
N475=1
N476=1
N477=1
N478=1
N479=1
N480=1
N481=1
N482=1
N483=1
N484=1
N485=1
N486=1
N487=1
N488=1
N489=1
N490=1
N491=1
N492=1
N493=1
N494=1
N495=1
N496=1
N497=1
N498=1
N499=1
N500=1
N501=1
N502=1
N503=1
N504=1
N505=1
N506=1
N507=1
N508=1
N509=1
N510=1
N511=1
N512=1
N513=1
N514=1
N515=1
N516=1
N517=1
N518=1
N519=1
N520=1
N521=1
N522=1
N523=1
N524=1
N525=1
N526=1
N527=1
N528=1
N529=1
N530=1
N531=1
N532=1
N533=1
N534=1
N535=1
N536=1
N537=1
N538=1
N539=1
N540=1
N541=1
N542=1
N543=1
N544=1
N545=1
N546=1
N547=1
N548=1
N549=1
N550=1
N551=1
N552=1
N553=1
N554=1
N555=1
N556=1
N557=1
N558=1
N559=1
N560=1
N561=1
N562=1
N563=1
N564=1
N565=1
N566=1
N567=1
N568=1
N569=1
N570=1
N571=1
N572=1
N573=1
N574=1
N575=1
N576=1
N577=1
N578=1
N579=1
N580=1
N581=1
N582=1
N583=1
N584=1
N585=1
N586=1
N587=1
N588=1
N589=1
N590=1
N591=1
N592=1
N593=1
N594=1
N595=1
N596=1
N597=1
N598=1
N599=1
N600=1
N601=1
N602=1
N603=1
N604=1
N605=1
N606=1
N607=1
N608=1
N609=1
N610=1
N611=1
N612=1
N613=1
N614=1
N615=1
N616=1
N617=1
N618=1
N619=1
N620=1
N621=1
N622=1
N623=1
N624=1
N625=1
N626=1
N627=1
N628=1
N629=1
N630=1
N631=1
N632=1
N633=1
N634=1
N635=1
N636=1
N637=1
N638=1
N639=1
N640=1
N641=1
N642=1
N643=1
N644=1
N645=1
N646=1
N647=1
N648=1
N649=1
N650=1
N651=1
N652=1
N653=1
N654=1
N655=1
N656=1
N657=1
N658=1
N659=1
N660=1
N661=1
N662=1
N663=1
N664=1
N665=1
N666=1
N667=1
N668=1
N669=1
N670=1
N671=1
N672=1
N673=1
N674=1
N675=1
N676=1
N677=1
N678=1
N679=1
N680=1
N681=1
N682=1
N683=1
N684=1
N685=1
N686=1
N687=1
N688=1
N689=1
N690=1
N691=1
N692=1
N693=1
N694=1
N695=1
N696=1
N697=1
N698=1
N699=1
N700=1
N701=1
N702=1
N703=1
N704=1
N705=1
N706=1
N707=1
N708=1
N709=1
N710=1
N711=1
N712=1
N713=1
N714=1
N715=1
N716=1
N717=1
N718=1
N719=1
N720=1
N721=1
N722=1
N723=1
N724=1
N725=1
N726=1
N727=1
N728=1
N729=1
N730=1
N731=1
N732=1
N733=1
N734=1
N735=1
N736=1
N737=1
N738=1
N739=1
N740=1
N741=1
N742=1
N743=1
N744=1
N745=1
N746=1
N747=1
N748=1
N749=1
N750=1
N751=1
N752=1
N753=1
N754=1
N755=1
N756=1
N757=1
N758=1
N759=1
N760=1
N761=1
N762=1
N763=1
N764=1
N765=1
N766=1
N767=1
N768=1
N769=1
N770=1
N771=1
N772=1
N773=1
N774=1
N775=1
N776=1
N777=1
N778=1
N779=1
N780=1
N781=1
N782=1
N783=1
N784=1
N785=1
N786=1
N787=1
N788=1
N789=1
N790=1
N791=1
N792=1
N793=1
N794=1
N795=1
N796=1
N797=1
N798=1
N799=1
N800=1
N801=1
N802=1
N803=1
N804=1
N805=1
N806=1
N807=1
N808=1
N809=1
N810=1
N811=1
N812=1
N813=1
N814=1
N815=1
N816=1
N817=1
N818=1
N819=1
N820=1
N821=1
N822=1
N823=1
N824=1
N825=1
N826=1
N827=1
N828=1
N829=1
N830=1
N831=1
N832=1
N833=1
N834=1
N835=1
N836=1
N837=1
N838=1
N839=1
N840=1
N841=1
N842=1
N843=1
N844=1
N845=1
N846=1
N847=1
N848=1
N849=1
N850=1
N851=1
N852=1
N853=1
N854=1
N855=1
N856=1
N857=1
N858=1
N859=1
N860=1
N861=1
N862=1
N863=1
N864=1
N865=1
N866=1
N867=1
N868=1
N869=1
N870=1
N871=1
N872=1
N873=1
N874=1
N875=1
N876=1
N877=1
N878=1
N879=1
N880=1
N881=1
N882=1
N883=1
N884=1
N885=1
N886=1
N887=1
N888=1
N889=1
N890=1
N891=1
N892=1
N893=1
N894=1
N895=1
N896=1
N897=1
N898=1
N899=1
N900=1
N901=1
N902=1
N903=1
N904=1
N905=1
N906=1
N907=1
N908=1
N909=1
N910=1
N911=1
N912=1
N913=1
N914=1
N915=1
N916=1
N917=1
N918=1
N919=1
N920=1
N921=1
N922=1
N923=1
N924=1
N925=1
N926=1
N927=1
N928=1
N929=1
N930=1
N931=1
N932=1
N933=1
N934=1
N935=1
N936=1
N937=1
N938=1
N939=1
N940=1
N941=1
N942=1
N943=1
N944=1
N945=1
N946=1
N947=1
N948=1
N949=1
N950=1
N951=1
N952=1
N953=1
N954=1
N955=1
N956=1
N957=1
N958=1
N959=1
N960=1
N961=1
N962=1
N963=1
N964=1
N965=1
N966=1
N967=1
N968=1
N969=1
N970=1
N971=1
N972=1
N973=1
N974=1
N975=1
N976=1
N977=1
N978=1
N979=1
N980=1
N981=1
N982=1
N983=1
N984=1
N985=1
N986=1
N987=1
N988=1
N989=1
N990=1
N991=1
N992=1
N993=1
N994=1
N995=1
N996=1
N997=1
N998=1
N999=1
N1000=1

```

# SECTION 5. A SAMPLE SORTING SECTION

FIGURE 31. COMPUTER PROGRAM SECTION FIVE



```

NE=NC-1
SIG=1.
ME=1.
CALL AVENER(E,E(1),NB,SIG,ME)
WRITE(6,220) ME,SIG
220 FORMAT (3X,'..... AVERAGE LASER ENERGY IS',F6.2,' ..... SIGMA EQUAL
1S',F6.2)
WRITE(6,7)
7 FORMAT (120X)

```

# SECTION 6.

```

SUBROUTINE AVENER (A,ST,NB,SIG,ME)
REAL*4 ME
REAL*4 A(500),AN(500),AS(500),SI(500)
AN(1)=ST
DO 200 J=2,NB
  JN1=J-1
  AN(J)=AN(JN1)+A(J)
  CCNT INUE
200 S=J
  ME=AN(J)/S
  AS(1)=A(1)-ME
  SI(1)=AS(1)**2
  DO 210 K=2,NB
    AS(K)=A(K)-ME
    KN1=K-1
    SI(K)=SI(KN1)+AS(K)**2
  CCNT INUE
210 SIG=(SI(K)/S)**.5
  RETURN
END

```

FIGURE 32. COMPUTER PROGRAM SECTION SIX AND SUBROUTINE AVENER



# LIST OF REFERENCES

1. Ames, W. F., Numerical Methods for Partial Differential Equations, p. 297, Barnes and Noble, Inc., 1969.
2. Antonov, A. V., Zaritskii, A. R., and Zakharov, S. D., "Collector Probe Measurements of the Parameters of a Laser Plasma at Long Distances," Soviet Journal of Quantum Electronics, v. 4, p. 342-344, Sep. 1974.
3. Baird, D. C., Experimentation: An Introduction of Measurement Theory and Experiment Design, F. 198, Prentice-Hall, Inc., 1962.
4. Baksht, F. G., et al., "Probe Measurements in a Cold, Dense, Highly Ionized Plasma," Soviet Physics - Technical Physics, v. 18, p. 1617-1622, June 1974.
5. Bar-Isaac, C., et al., "Thermal Structure of the Evaporation Front in Laser Drilling Processes," Applied Physics, v. 5, p. 121-125, 1974.
6. Bascv, N. G., et al., "Heating and Decay of Plasma Produced by a Giant Laser Pulse Focused on a Solid Target," Soviet Physics JETP, v. 24, p. 659-666, Apr. 1967.
7. Bascv, N. G., et al., "High Temperature Effects of Intense Laser Emission Focused on a Solid Target," Soviet Physics JETP, v. 24, p. 575-582, Oct. 1968.
8. Bechtel, J. H., "Heating of Solid Targets with Laser Pulses," Journal of Applied Physics, v. 46, p. 1585-1593, Apr. 1975.
9. Botka, N., Discussions with; at China Lake Michaelson Laboratory, Subj: Equipment Layout for Laser Interaction Experiments, on 3 Mar. 1976.
10. Brocks, K. M., An Investigation of Early Disturbances Focud in Association with Laser Produced Plasmas, M. S. Thesis, U. S. Naval Postgraduate School, Monterey, California, 1973.
11. Bykovskii, Yu. A., et al., "Neutral Particles from the Interaction of Laser Radiation with a Solid





Target," Soviet Physics - Technical Physics, v. 19,  
p. 1635, June 1975.

12. Carslaw, H. S., and Jaeger, J. C., Conduction of Heat in Solids, 2nd ed., p. 282-296, Oxford University Press, 1959.
13. Chen, F. F., Introduction to Plasma Physics, Plenum Press, p. 370-372, 1974.
14. Chung, F. M., Talbot, L., and Tcuryan, K. J., "Electric Probes in Stationary and Flowing Plasmas: Part I. Collisionless and Transitional Probes," AIAA Journal, v. 12, p. 133-144, Feb. 1974.
15. Churg, F. M., et al., "Part 2 Continuum Probes," AIAA Journal, v. 12, p. 144-154, Feb. 1974.
16. Davis, I. J., Self-Generated Magnetic Fields Produced by Laser Bombardment of a Solid Target, M. S. Thesis, U. S. Naval Postgraduate School, Monterey, California, 1971.
17. Demtroder, W., and Jantz, W., "Investigation of Laser Produced Plasmas from Metal Surfaces," Plasma Physics, v. 12, p. 691-703, 1970.
18. Eyni, M. and Cuperman, S., "A Method for Determination of Relative Densities in a Low-Density Plasma by Electric Probes," Plasma Physics, v. 12, p. 77-81, 1970.
19. Fox, J. A., "A Method for Improving Continuous Wave Laser Penetration of Metal Targets," Applied Physics Letters, v. 26, p. 682-684, 15 June 1975.
20. Frank-Kamenetskii, D. A., Plasma, The Fourth State of Matter, p. 159, Plenum Press, 1972.
21. Ghez, F. A., and Laff, R. A., "Laser Heating and Melting of Thin Films on a Low Conductivity Substrate," Journal of Applied Physics, v. 46, p. 2103-2110, May 1975.
22. Gottfried, B. S., Programming with Fortran IV, p. 272, Quantum Publishers, Inc., 1972.
23. Gregg, D. W., and Thomas, S. J., "Kinetic Energies of Ions Produced by Giant Laser Pulses," Journal of Applied Physics, v. 37, p. 4313-4316, Nov. 1966.
24. Honig, F. E., "Laser-Induced Emission of Electrons and Positive Ions from Metals and Semi-Conductors," Applied Physics Letters, v. 3, p. 8-13, July 1963.
25. Huddleston, R. H. and Leonard, S. I., eds. Plasma Diagnostic Techniques, p. 627, Academic Press, 1965.



26. Inoue, N., Kawasumi, U., and Miyamoto, K., "Expansion of a Laser Produced Plasma into a Vacuum," Plasma Physics, v. 13, p. 84-87, 1971.
27. Isegor, N. R., "Effect of Background Gas on Laser Induced Electron Emission from Metal Surfaces," Journal of Applied Physics, v. 36, p. 316-317, Jan. 1965.
28. Johnson, E. C. and Malter, L., "A Floating Double Probe Method for Measurements in Gas Discharge," Physical Review, v. 80, p. 58-68, Oct. 1950.
29. Kitsunozaki, A., Tanimoto, M., and Sekiguchi, T., "Properties of Plasma Produced by a Laser Pulse from a Freely Falling Deuterium Ice-Pellet," Plasma Physics, v. 17, p. 875-885, 1975.
30. Krckhin, O. N., "High-Temperature and Plasma Phenomena Induced by Laser Radiation," Physics of High Energy Density, eds. P. Caldirola and H. Knoepfel, p. 278-305, Academic Press, 1971.
31. Langmuir, I., "The Interaction of Electron and Positive Ion Space Charges in Cathode Sheaths," Physical Review, v. 33, p. 954-974, June 1929.
32. Lawrence Livermore Laboratory Report UCRL-76600, Fast Ion Generation in Laser-Plasma Interactions, by E. J. Valeo and I. B. Bernstein, p. 14, 31 Mar. 1975.
33. Lindberg, L. and Kristoferson, L., "Electric Probe Measurements in a Moving and Magnetized Plasma," Plasma Physics, v. 12, p. 831-838, 1970.
34. Mairan, T. H., "Optically Pumped Solid State Lasers," Solid State Design, v. 4, p. 17-21, 1963.
35. Morrison, R., Grounding and Shielding Techniques in Instrumentation, p. 144, John Wiley and Sons, Inc., 1967.
36. Mott-Smith, H. M. and Langmuir, I., "The Theory of Collectors in Gaseous Discharges," Physical Review, v. 2, p. 727-735, Oct. 1926.
37. Naval Research Laboratory, Report No. NRL-MR-2904, Laser Target Model, by D. G. Colombant, et al., p. 38, Dec. 1974.
38. Naval Research Laboratory, Report No. NRL-MR-2931, A Model for the Production and Transport of Energetic Particles in a Laser Produced Plasma, by W. M. Manheimer, et al., p. 11, Mar. 1975.
39. Naval Research Laboratory, Report No. NRL-7728, Response of Materials to Laser Radiation: A Short



Course, by J. T. Schriempf, p. 73, July 1974.

40. Clstad, R. A. and Olander, D. R., "Evaporation of Solids by Laser Pulses, I. Iron," Journal of Applied Physics, v. 46, p. 1499-1508, Apr. 1975.
41. Porteus, J., Discussions with, at China Lake Michaelson Laboratory, 3 Mar. 1976. Subj: Response of Aluminum Targets to Laser Pulses of Various Energies.
42. Ready, J. F., Effects of High Power Laser Radiation, p. 433, Academic Press, 1971.
43. Ready, J. F., "Development of Plume of Material Vaporized by Giant-Pulsed Laser," Applied Physics Letters, v. 3, p. 11-13, July 1963.
44. McKee, I. L., An Investigation of the Self-Generated Magnetic Fields Associated with a Laser-Produced Plasma, Ph. D. Thesis, U.S. Naval Postgraduate School, Monterey, California, 1972.
45. Rusakov, V. D., Modern Plasma Research Methods, p. 207, AEC Report No. AEC-tr-6348, Apr. 1964.
46. Schwirzke, F., Measurements of Spontaneous Magnetic Fields in Laser Produced Plasmas, paper presented at the third workshop on "Laser Interactions and Related Plasma Phenomena," Rensselaer Polytechnic Institute, Troy, New York, 13-17 Aug. 1973.
47. Schwirzke, F., and Cooper, A. W., Research in Plasma Physics, NAVAIRSYSCOMAIR Task No. A3110/551/69R0080201, p. 14, 15 Dec. 1969.
48. Sharpire, L. F., and Allen, R. C., Numerical Computing: An Introduction, p. 258, W. B. Saunders Co., 1973.
49. Shewchuk, S. A., X-Ray Diagnostics of Laser Produced Aluminum Plasmas, M.S. Thesis, U.S. Naval Postgraduate School, Monterey, California, 1976.
50. Smith, G. E., Numerical Solution of Partial Differential Equations with Exercises and Worked Solutions, p. 179, Oxford University Press, 1965.
51. Spiegel, M. R., Theory and Problems of Calculus of Finite Differences and Difference Equations, p. 259, McGraw-Hill, 1971.
52. Steverding, E., "Ignition of Laser Detonation Waves," Journal of Applied Physics, v. 45, p. 3507-3511, Aug. 1974.
53. Swift, J. D., and Schwar, M. J. R., Electrical Probes for Plasma Diagnostics, p. 334, American Elsevier





Publishing Co., 1969.

54. Sykcvskii, Yu. A., et al., "Neutral Particles from the Interaction of Laser Radiation with a Solid Target," Soviet Physics - Technical Physics, v. 19, p. 1635, June 1975.
55. Tonks, I. and Langmuir, I., "A General Theory of the Plasma of an Arc," Physical Review, v. 34, p. 876-895, Sep. 1929.
56. Tonks, I., and Langmuir, I., "Oscillations in Ionized Gases," Physical Review, v. 33, p. 195-210, Feb. 1929.
57. Union Carbide Electronics, KORAD Laser Systems Instruction Manual for Nd:glass Laser five volumes, KORAD Department, Santa Monica, California, 1969.
58. Vincent, J., and Godard, R., "Spherical Langmuir Probe: Complements to the Classical Theory," Plasma Physics, v. 14, p. 793-803, 1972.
59. Wei, F. S. F., Nelson, D. J., and Hall, R. B., "Laser Induced Evaporation of Solid Surfaces," Journal of Chemical Physics, v. 62, p. 3050-3051, Apr. 1975.
60. Wharton, C. E., and Trivelpiece, A. W., "Waves in Laboratory Plasmas," Plasma Physics in Theory and Application, ed. by W. B. Kunkel, p. 245, McGraw Hill, 1966.
61. Williamsen F., Laser Generated Magnetic Fields, M. S. Thesis, U.S. Naval Postgraduate School, Monterey, California, 1976.





# INITIAL DISTRIBUTION LIST

	No. Copies
1. Defense Documentation Center Cameron Station Alexandria, Virginia 22314	2
2. Library, Code 0212 Naval Postgraduate School Monterey, California 93940	2
3. Department Chairman, Code 61Wh Department of Physics and Chemistry Naval Postgraduate School Monterey, California 93940	2
4. Asst Prof F.B. Schwirzke, Code 61Sw (thesis adv) Department of Physics and Chemistry Naval Postgraduate School Monterey, California 93940	2
5. Professor A.W. Cooper, Code 61Cr (thesis advisor) Department of Physics and Chemistry Naval Postgraduate School Monterey, California 93940	2
6. LT Daniel J. Callahan, USN (student) 1433 NE 24 Court Ft. Lauderdale, Florida 33305	1







Thesis  
C18873  
c.1

Callahan  
Laser plasma particle  
velocities.

166520

NOV 8 85

23738  
29605

ies

Thesis  
C18873  
c.1

Callahan  
Laser plasma particle  
velocities.

166520

thesC18873

Laser plasma particle velocities.



3 2768 002 08450 1

DUDLEY KNOX LIBRARY